

FraGNNet: A Deep Probabilistic Model for Tandem Mass Spectrum Prediction

Anonymous authors

Paper under double-blind review

Abstract

Compound identification from tandem mass spectrometry (MS/MS) data is a critical step in the analysis of complex mixtures. Typical solutions for the MS/MS spectrum to compound (MS2C) problem involve comparing the unknown spectrum against a library of known spectrum-molecule pairs, an approach that is limited by incomplete library coverage. Compound to MS/MS spectrum (C2MS) models can improve retrieval rates by augmenting real libraries with predicted MS/MS spectra. Unfortunately, many existing C2MS models suffer from problems with mass accuracy, generalization, or interpretability. We develop a new probabilistic method for C2MS prediction, FraGNNet, that can efficiently and accurately simulate MS/MS spectra with high mass accuracy. Our approach formulates the C2MS problem as learning a distribution over molecule fragments. FraGNNet achieves state-of-the-art performance in terms of prediction error and surpasses existing C2MS models as a tool for retrieval-based MS2C.

1 Introduction

Small molecule identification is a challenging problem with broad scientific implications. Determining the chemical composition of a liquid sample (such as human blood or plant extract) is a critical step both in the discovery of novel compounds and in the recognition of known compounds in new contexts. Tandem mass spectrometry (MS/MS) is a widely employed tool for molecule identification, with applications ranging from drug discovery to environmental science and metabolomics (Dueñas et al., 2022; Gowda & Djukovic, 2014; Peters, 2011; Lebedev, 2013). Analyzing the set of MS/MS spectra measured from a liquid sample can reveal important information about its chemical constitution: each spectrum acts as a chemical signature that can help identify a molecule in the sample.

The MS/MS spectrum to compound (MS2C) problem is the task of inferring the structure of a molecule from its mass spectrum. Existing MS2C workflows often rely on comparing the spectrum of an unknown molecule against a library of reference MS/MS spectra with known identities. However, spectral libraries are far from comprehensive. The largest public MS/MS library, NIST23 (Stein, 2023), consists of 51,501 compounds and 2.4 million spectra. In contrast, the most commonly used chemical database, PubChem (Kim et al., 2019), contains 119 million compounds at the time of writing. The huge gap in spectrum coverage means *retrieval-based* MS2C might not work even for molecules that have previously been observed.

Many computational approaches attack the MS2C problem head-on by attempting to predict information about the molecule from the MS/MS spectrum. Some models infer high-level chemical properties from the spectrum (Dührkop et al., 2015; Voronov et al., 2022) and use these features to recommend likely candidate structures from existing chemical databases (Dührkop et al., 2015; Dührkop et al., 2019; Goldman et al., 2023b;c; Bushuiev et al., 2025) or guide generative models towards potential matches (Stravs et al., 2022). Other methods (Butler et al., 2023; Shrivastava et al., 2021; Wang et al., 2025; Bohde et al., 2025) directly generate structures from the spectrum.

Compound to mass spectrum (C2MS) prediction can be viewed as an indirect approach for solving the MS2C problem. Instead of attempting to infer structural features from the MS/MS spectrum, C2MS models work by boosting the effectiveness of existing retrieval-based MS2C workflows. Accurate C2MS models can predict

MS/MS spectra for millions of molecules that are missing from spectral libraries, improving coverage by orders of magnitude. This kind of library augmentation has been a mainstay in retrieval-based MS2C workflows for over a decade (Wolf et al., 2010; Allen et al., 2015; Wishart et al., 2018) and has led to the successful identification of many novel compounds (Skinnider et al., 2021; Wang et al., 2023; Qiang et al., 2024).

Despite numerous advances, challenges with C2MS remain (Schymanski et al., 2017; Bushuiev et al., 2024). Many existing approaches cannot predict MS/MS spectra with high mass accuracy; this loss of information can be harmful in MS2C applications (Kind et al., 2018). Model interpretability is important for manual validation of MS/MS predictions, yet many models operate as black boxes. Finally, generalization to new compounds is difficult given the limited availability of training data.

In this work, we make the following contributions:

- We introduce FraGNNNet, a novel method for MS/MS spectrum prediction that integrates combinatorial bond-breaking methods with principled probabilistic modelling.
- We argue that this approach meets key requirements in the areas of prediction error, mass accuracy and interpretability.
- Through comparisons with strong baseline models, we demonstrate that FraGNNNet achieves state-of-the-art performance on MS/MS spectrum prediction and compound retrieval tasks.

2 Background

At a high level, MS/MS spectrometry provides information about a molecule’s structure by measuring how it breaks down. The experimental process is outlined in Figure 1. First, molecules in the sample are ionized: at this stage they are referred to as *precursor ions*, because they have not yet undergone fragmentation. In liquid samples, each molecule may become associated with a charged *adduct* during ionization. For example, if the adduct is a hydrogen ion H^+ , an $[M+H]^+$ precursor ion will form. Following ionization, the mass to charge ratio (m/z) of each precursor ion is subsequently measured using a mass analyzer. Once the precursor m/z values have been measured, ions of a selected m/z are isolated and subjected to fragmentation for further analysis. The fragmentation process is typically facilitated by energetic collisions with neutral gas particles, and is influenced by experimental parameters such as *collision energy*. In general, higher collision energy results in more extensive fragmentation.

A *fragment* is defined as a molecule composed of a subset of the atoms in the original precursor molecule. The fragmentation process involves chemical reactions that cause the stochastic breakage and formation of bonds in the molecule. After fragmentation, the resulting fragment ions are sent back to the mass analyzer for m/z measurement, producing a distribution over m/z values that is called the MS/MS spectrum. It is possible for different fragments to have nearly identical m/z , complicating analysis of the spectrum. Throughout this work, we focus our analysis on $[M+H]^+$ spectra: as z is always +1, the spectrum can be directly interpreted as a distribution over masses. However, our methods can be trivially extended to many other types of adducts.

Mathematically, an MS/MS spectrum Y can be represented as a finite set of pairs $\{(m_j, P(m_j))\}_j$ where each mass m_j has an associated probability $P(m_j)$. We refer to each individual pair $(m_j, P(m_j))$ as a *peak*, where the mass m_j (measured in Daltons or Da) is called the peak *location* and the probability $P(m_j)$ is called the peak *intensity*. The precision of the peak locations is commonly referred to as the *mass accuracy*. The C2MS problem can be formulated as a standard supervised learning task. The dataset is composed of N tuples $\{(X_i, Y_i)\}_{i=1}^N$ where X_i is a molecule and Y_i is its associated MS/MS spectrum. The goal of a C2MS model is to predict Y_i from X_i . The set of masses in a particular spectrum Y_i is denoted as M_i .

Every molecule can be represented as an undirected *molecular graph* $G = (V, E)$. Each node $a \in V$ represents an atom in the molecule with an associated element label $\omega_a \in \Omega$ (where $\Omega = \{C, H, N, O, P, S, \dots\}$ is a finite set of common elements) and each edge $b \in E$ represents a covalent bond between atoms. A *molecular formula* is a representation of the molecule that captures only the quantity of each type of atom present in the graph. For example, the molecule methylaminomethanol (Figure 6) has a molecular formula of C_2H_7NO , which means that its molecular graph contains two carbon atoms, seven hydrogens, one nitrogen, and one oxygen.

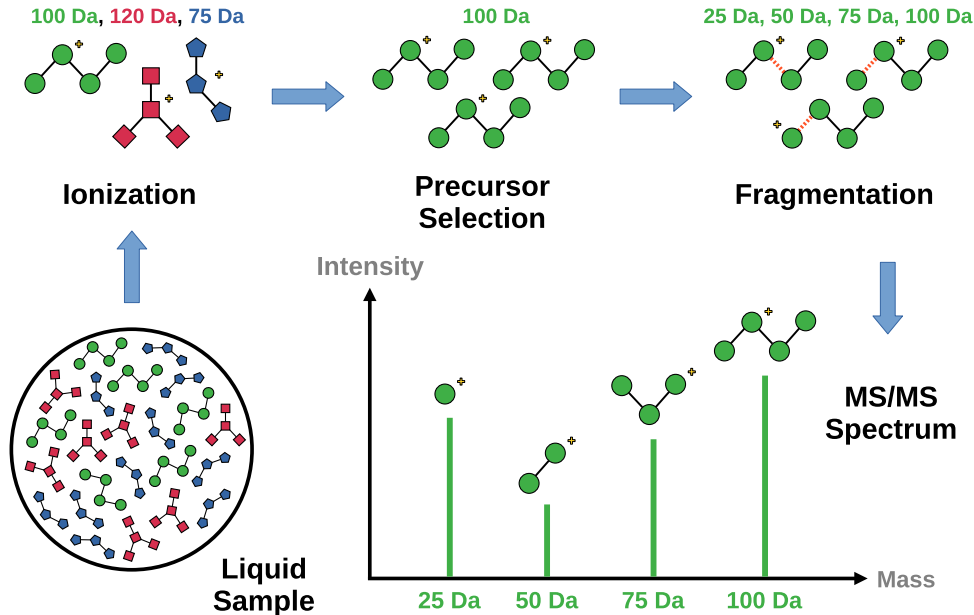


Figure 1: Overview of MS/MS spectrometry: molecules in the sample are ionized to form precursors, filtered by precursor mass (100 Da), and sent for fragmentation. The fragmentation process stochastically produces fragments with mass values of 25, 50, 75 Da. The distribution of precursor and fragment mass values forms the spectrum.

Peak annotation is the process of linking peaks in an MS/MS spectrum to chemical information. Practitioners often use these annotations to interpret the spectrum: in the context of MS2C, these annotations can help users compare possible candidate molecules by facilitating the incorporation of domain knowledge (Steckel & Schlosser, 2019; Johnson & Carlson, 2015). When a peak is associated with a subformula of the precursor molecular formula, this is called a *formula annotation*; similarly, when a peak is associated with a fragment of the precursor molecule this is called a *fragment annotation*.

3 Related Work

The increasing availability of small molecule MS/MS data has lead to a proliferation of machine learning models for C2MS prediction. Existing methods can be broadly grouped into two categories, *binned* and *structured*, based on how they represent the spectrum.

Binned methods approximate the spectrum by discretizing the mass range into a fixed number of equally sized bins, each with an associated intensity. This simplifies the spectrum prediction problem to a vector regression task, which can be readily solved without extensive domain-specific model customization. Binned approaches generally vary based on the strategy they employ for encoding the input molecule: multi-layer perceptrons (Wei et al., 2019), 2D and 3D graph neural networks (Zhu et al., 2020; Li et al., 2022; Hong et al., 2023; Park et al., 2024), and graph transformers (Young et al., 2023) have all been used successfully. However, selecting an appropriate bin size can be challenging: bins that are too large result in loss of information, while bins that are too small can be overly sensitive to measurement error and yield high-dimensional output vectors.

Structured approaches sidestep the binning problem by modelling the spectrum as a distribution over chemical formulae. This representation allows for arbitrarily high mass accuracy, since the formula masses can be used to determine peaks locations with precision. Some methods predict the formula distribution directly, using either autoregressive formula generation (Goldman et al., 2023a) or a large fixed formula vocabulary (Murphy et al., 2023). Others rely on recursive fragmentation (Wang et al., 2021; Zhu & Jonas, 2023; Nowatzky et al., 2025) or autoregressive generation (Goldman et al., 2024) to first model a distribution over fragments, then

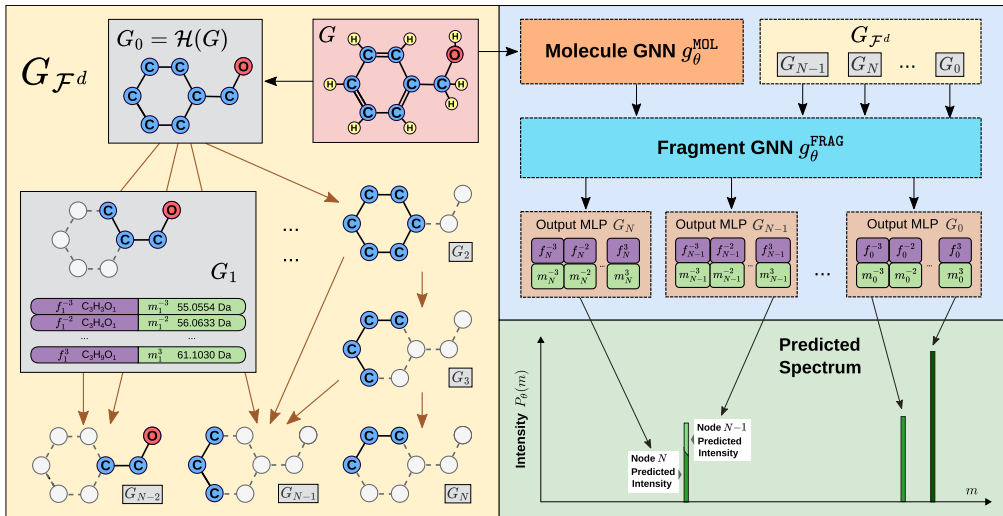


Figure 2: Overview of the FraGNNet C2MS model. The input molecule (G , red box) is processed into an approximate Fragmentation DAG ($G_{\mathcal{F}^d}$, yellow box) and independently embedded by the Molecule GNN (g_{θ}^{MOL} , orange box). Information from the DAG is combined with the molecule embedding and processed by the Fragment GNN (g_{θ}^{FRAG} , blue box). Output MLPs (brown boxes) are applied to each fragment node n in the DAG to predict a per-node distribution over formulae (purple boxes), which can be mapped to a distribution over masses (green boxes) and summed across nodes to create the MS/MS spectrum.

map this to a distribution over formulae. Structured C2MS models tend to be more interpretable, since each peak is always associated with a formula (and possibly one or more fragments). However, they can also be slower than binned approaches due to the increased complexity of the spectrum representation.

CFM-ID (Allen et al., 2015; Wang et al., 2021) and ICEBERG (Goldman et al., 2024) are structured C2MS models that explicitly model fragmentation. Like FraGNNet, both approaches algorithmically generate fragments (substructures) of the input molecule and predict a distribution over those fragments. Their principal distinction, however, lies in the specific strategy for fragment generation. CFM-ID employs a deterministic bond-breaking algorithm and incorporates chemistry domain knowledge to compute a set of plausible fragments. This approach benefits from consistent fragment generation and strong chemical priors; however, it does not scale well to larger molecules and datasets. In contrast, ICEBERG uses a learned model to autoregressively generate fragments. This approach has proven to be overall more accurate and scalable than CFM-ID (Goldman et al., 2024), but it relies on a stochastic fragment generation process that can result in errors. FraGNNet takes a pragmatic approach: like CFM-ID, it employs a deterministic algorithm to generate a comprehensive set of fragments; however, by relaxing chemical constraints it can achieve greater efficiency and scale to larger compounds like ICEBERG.

4 Methods

4.1 Overview

The goal of our method is to predict the MS/MS spectrum for an input molecular structure. The model works in two stages: first, a recursive bond-breaking algorithm (Section 4.2) generates a set of plausible molecule fragments. Then, a probabilistic model (Section 4.3) parameterized by a graph neural network (Section 4.4) predicts a distribution over these fragments. The fragment distribution induces a distribution over molecular formulae, which is converted to an MS/MS spectrum using formula masses (Section 4.3). This approach allows for extremely high mass accuracy and probabilistic formula and fragment annotations.

4.2 Recursive Fragmentation

Recall our definition of the molecular graph $G = (V, E)$ from Section 2, where nodes $a \in V$ represents atoms and edges $b \in E$ represent bonds. Let $S(G)$ be the set of connected subgraphs of the graph G .

Definition 4.1. The graph $\mathcal{F}(G) = (\mathcal{F}_1(G), \mathcal{F}_2(G))$ is called a fragmentation DAG with respect to the graph G if the following properties hold:

1. Each node $n \in \mathcal{F}_1(G)$ corresponds to a connected subgraph $G_n \in S(G)$
2. Each edge $e \in \mathcal{F}_2(G)$ from node $u \in \mathcal{F}_1(G)$ to node $v \in \mathcal{F}_1(G)$ exists if and only if $G_v \in S(G)$ is a connected subgraph of $G_u \in S(G)$ that can be constructed by removing a single edge from G_u and selecting one of the resulting connected subgraphs.

Note that the root node r of $\mathcal{F}(G)$ always corresponds to the original graph G , and the leaves of $\mathcal{F}(G)$ correspond to individual atoms $a \in V$.

Our method assumes that most fragments that contribute to an MS/MS spectrum can be modelled as products of a sequence of bond breakages. Such fragments appear as nodes $n \in \mathcal{F}_1(G)$, and their fragmentation history can be represented as a path from the root r to n . We can derive a set of molecular formulae $\{f_n : n \in \mathcal{F}_1(G)\}$, where each f_n represents the molecular formula of G_n . This set can be used to calculate the set of possible peak locations in the spectrum, $M(G) = \{m_n : n \in \mathcal{F}_1(G)\}$ where $m_n = \text{mass}(f_n)$ is the monoisotopic mass of molecular formula f_n .

The fragmentation DAG $\mathcal{F}(G)$ can be a useful tool for spectrum prediction (Wang et al., 2021; Goldman et al., 2023a; 2024), providing information about peak locations and relationships between fragments in the spectrum. However, computing $\mathcal{F}(G)$ from G through exhaustive edge removal is expensive, requiring $\mathcal{O}(2^{|E|})$ operations. Inspired by previous approaches from the literature (Wolf et al., 2010; Ruttkies et al., 2016; Allen et al., 2015; Ridder et al., 2014; Goldman et al., 2024), we approximate $\mathcal{F}(G)$ using a few simplifying assumptions.

Definition 4.2. The graph $\mathcal{H}(G) = (\mathcal{H}_1(G), \mathcal{H}_2(G))$ is called a heavy atom skeleton of G if $\mathcal{H}(G)$ is the largest connected subgraph of G such that $\omega_a \neq \text{H}$ (hydrogen) for all $a \in \mathcal{H}_1(G)$.

Since $|\mathcal{H}_2(G)|$ is often smaller than $|E|$ (in the NIST20 MS/MS dataset, $\approx 43\%$ smaller on average), calculating $\mathcal{F}(\mathcal{H}(G))$ is considerably faster than calculating $\mathcal{F}(G)$. We employ a recursive edge removal (*i.e.*, bond-breaking) algorithm that only considers nodes that are at most d hops away from the root r , producing a connected subgraph $\mathcal{F}^d(\mathcal{H}(G))$ of $\mathcal{F}(\mathcal{H}(G))$ (see Algorithm 1 for details about our implementation).

For simplicity of notation, we refer to $\mathcal{F}^d(\mathcal{H}(G))$ as $G_{\mathcal{F}^d}$, with vertex set $V_{\mathcal{F}^d}$ and edge set $E_{\mathcal{F}^d}$. By definition, each node $n \in V_{\mathcal{F}^d}$ is associated with a fragment subgraph $G_n \in S(\mathcal{H}(G))$ that does not contain any hydrogen atoms. Since real fragments often include hydrogens, we employ heuristics to bound the number of hydrogens associated with each G_n . This approach enables us to account for hydrogens while avoiding the computational cost of explicitly modeling their positions in the graph.

Let h_n be the number of hydrogen atoms in original molecular graph G that are connected to an atom in the fragment subgraph G_n . We define the set $\{h_n - j, \dots, h_n + j\}$ as the range of hydrogen counts for the subgraph G_n , where j is an (integer) tolerance parameter. This induces a set of possible molecular formulae $\{f_n^{-j}, \dots, f_n^j\}$ and associated masses $\{m_n^{-j}, \dots, m_n^j\}$, where f_n^i is f_n with the addition of $h_n + i$ hydrogens, and m_n^i is its corresponding mass. For example, if $f_n = \text{C}_2\text{O}_1$, $h_n = 3$, and $i = 2$, then $m_n^i = \text{mass}(\text{C}_2\text{O}_1\text{H}_5) = 178.0477$ Da.

Definition 4.3. The set

$$\hat{M}(G, d, j) = \bigcup_{n \in V_{\mathcal{F}^d}} \{m_n^{-j}, \dots, m_n^j\}$$

is the set of masses derived from the approximate heavy-atom fragmentation DAG $G_{\mathcal{F}^d}$ with hydrogen tolerance j .

Empirically, we find that calculating $\hat{M}(G, d, j)$ (Definition 4.3) with $d \in \{3, 4\}$ and $j = 4$ can effectively capture most of the total peak intensity in real MS/MS data (see Table 3).

4.3 Probabilistic Formulation

Our model can be interpreted as a hierarchical latent variable model, whose latent distributions depend on a molecular graph G and its approximate fragmentation DAG $G_{\mathcal{F}^d}$.

To begin, we define the following latent probability distributions:

Definition 4.4. Let $P_\theta(n)$ be a discrete finite probability distribution over the DAG nodes $N = V_{\mathcal{F}^d}$, parameterized by a neural network g_θ .

Definition 4.5. Let $P_\theta(f|n)$ be a discrete finite conditional distribution between DAG nodes N and associated formulae $F = \bigcup_{n \in N} \{f_n^{-j}, \dots, f_n^j\}$, parameterized by a neural network g_θ .

Both distributions depend implicitly on the molecular graph G , but for clarity of notation we have omitted this. Note that for each node n , $P_\theta(f|n)$ has support over $2j + 1$ formulae.¹

The joint distribution $P_\theta(n, f) = P_\theta(n) P_\theta(f|n)$ can be loosely interpreted as identifying which substructures are generated during fragmentation, with $P_\theta(n)$ modelling the heavy atom structures of the probable fragments and $P_\theta(f|n)$ modelling the number of hydrogens associated with each of those fragments.

By marginalizing $P_\theta(n, f)$ over the nodes n , it is possible to calculate a distribution over molecular formulae $P_\theta(f)$. Since each formula f has an associated mass, the discrete distribution $P_\theta(f)$ can be easily converted to a continuous distribution $P_\theta(m)$ over masses. Following Allen et al. (2015), we formulate $P_\theta(m)$ as a mixture of truncated univariate Gaussians as outlined in Equation 1:

$$P_\theta(m) = \sum_f P_\theta(f) P(m|f) \quad (1)$$

The conditional $P(m|f)$ is a narrow truncated Gaussian centered on the formula mass, $\mu(f) = \text{mass}(f)$, with variance $\sigma(f)$ proportional to f and truncation occurring at ± 1 standard deviation from the mean. This Gaussian model approximates the error distribution of the mass analyzer (Allen et al., 2015). At inference time it is convenient to approximate $P(m)$ as a discrete distribution with $P(m|f) = \delta(\text{mass}(f))$, where δ is the Dirac delta function.

Using Bayes Theorem, we can calculate another latent distribution $P_\theta(n|f)$ that identifies how much each fragment n is contributing to a predicted peak centered at formula f . We use $P_\theta(n|f)$ to predict fragment annotations for each output peak (see Figure 3 and Section 5.4).

In Appendix A.3, we describe analogs of $P_\theta(n)$, $P_\theta(f|n)$, and $P_\theta(n|f)$ that account for fragment subgraph isomorphism.

4.4 Neural Network Parameterization

The distributions $P_\theta(n)$ and $P_\theta(f|n)$ are parameterized by a two-stage graph neural network (GNN, Battaglia et al. 2018) as defined by Equation 2:

$$g_\theta(G, G_{\mathcal{F}^d}) = g_\theta^{\text{FRAG}}(g_\theta^{\text{MOL}}(G), G_{\mathcal{F}^d}) \quad (2)$$

The first stage g_θ^{MOL} , called the *Molecule GNN*, operates on the input molecular graph G . The second stage g_θ^{FRAG} , called the *Fragment GNN*, combines information from the fragmentation DAG and the molecule embeddings to predict the distributions $P_\theta(n)$ and $P_\theta(f|n)$.

¹There is additional filtering for chemical validity which may remove some formulae, but for clarity this has been omitted.

4.4.1 Molecule GNN

The Molecule GNN g_{θ}^{MOL} takes the input molecular graph G and outputs embeddings for the atoms in the graph. The atom embeddings $\bar{h}_a^{(0)}$ and bond embeddings $\bar{h}_b^{(0)}$ are initialized with specific features from G (see Appendix A.4).

GNN models work by iteratively updating node states through the aggregation of neighbourhood information. g_{θ}^{MOL} uses the GINE architecture (Xu et al., 2019; Fey & Lenssen, 2019), which incorporates both node and edge information in its updates. The GINE update rule is given by equation 3, where l is the GNN layer index, $l \in \{1, \dots, L_1\}$, and q_{θ} is a standard multi-layer perceptron (MLP):

$$\bar{h}_a^{(l+1)} = q_{\theta} \left(\bar{h}_a^{(l)} + \sum_{u \in \mathbb{N}(a)} \text{ReLU}(\bar{h}_u^{(l)} + \bar{h}_b^{(l)}) \right) \quad (3)$$

The final atom embeddings $\bar{h}_a^{(L_1)}$ are subsequently passed to the Fragment GNN g_{θ}^{FRAG} for further processing.

4.4.2 Fragment GNN

The Fragment GNN g_{θ}^{FRAG} is another GINE network that propagates information along the approximate fragmentation DAG. Each DAG node $n \in V_{\mathcal{F}^d}$ is featurized using information about its associated subgraph G_n , precisely described in Equations 4 and 5. The vector $\bar{h}_n^{(0)}$ is a concatenation of three terms: \hat{h}_n^s is the average atom embedding for atoms in G_n ; \hat{h}_n^f is an embedding of the subgraph formula f_n ; and \hat{h}_n^d is an embedding of the depth in the DAG at which node n is located.

$$\bar{h}_n^{(0)} = \hat{h}_n^s \parallel \hat{h}_n^f \parallel \hat{h}_n^d \quad (4)$$

$$\hat{h}_n^s = \frac{1}{|V_n|} \sum_{a \in V_n} \bar{h}_a^{(L_1)} \quad (5)$$

The edge embeddings $\bar{h}_e^{(0)}$ are also initialized with subgraph information: they capture differences between adjacent DAG nodes. Refer to Appendix A.5 for full details.

The DAG nodes are processed by the Fragment GNN in a manner that is similar to Equation 3. After L_2 layers of processing, a small output MLP is applied to each node embedding $\bar{h}_n^{(L_2)}$, producing a $2j + 1$ dimensional vector representing the unnormalized logits for $P_{\theta}(n, f_n^i)$ for each $i \in \{-j, \dots, j\}$. The other latent distributions in Section 4.3 are calculated from the joint through normalization, marginalization, and application of Bayes Theorem.

After performing model ablations (see Appendix A.8), we discovered that edge information could be omitted without degradation in performance, allowing for faster training and inference. As a result, the experiments in Section 5 used a variant of g_{θ}^{FRAG} that excludes the neighbourhood aggregation term from the GINE update, effectively acting as a node-wise MLP.

4.5 Loss Function

We fit the parameters of the model θ with maximum likelihood estimation, using stochastic gradient descent. The loss function is based on the negative log-likelihood of the data, defined in Equation 6:

$$\mathcal{L}_{\text{NLL}}(\theta) = \frac{1}{I} \sum_{i=1}^I \sum_{m \in M_i} -P(m) \log P_{\theta}(m) \quad (6)$$

For each spectrum (indexed by i), a subset of the peak masses $M_i^{\text{OS}} \subseteq M_i$ are defined to be *Outside of the Support (OS)* if they are far enough from away the predicted set of masses $\hat{M}(G_i, d, j)$ such that their predicted probability is 0 (Equation 7).

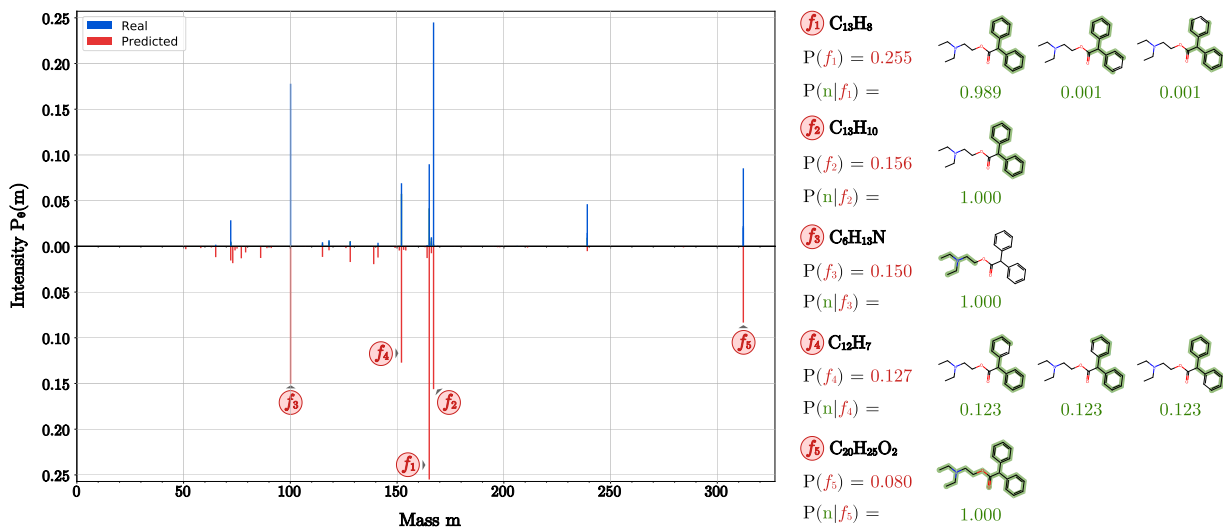


Figure 3: Example Spectrum Prediction with Peak Annotations: A real spectrum (blue) for a molecule from the test set, Adiphenine, is compared with its corresponding FraGNNNet-D4 prediction (red). The five most intense peak predictions are annotated with formulae and up to three probable fragment structures. The fragment annotation for peak 5 clearly corresponds to the precursor ion (*i.e.*, the entire graph). The model is uncertain about the fragment annotation for peak 4, giving equal probability (0.123) to three related structures and significant probability (0.631) to other less likely structures.

The rest of the masses $M_i^{IS} = M_i - M_i^{OS}$ are deemed to be *Inside of the Support (IS)*.

$$P(M_i^{OS}) = \sum_{m \in M_i: P_\theta(m)=0} P(m) \quad (7)$$

Modelling the OS probability can provide useful information about the reliability of the predicted spectrum (Appendix A.7). FraGNNNet is trained to predict $P_\theta(M_i^{OS})$, an estimation of $P(M_i^{OS})$. Adjusting the loss function $\mathcal{L}_{MLL}(\theta)$ to incorporate the OS cross-entropy term yields Equation 8:

$$\mathcal{L}(\theta) = \frac{1}{I} \sum_{i=1}^I \sum_{m \in M_i^{IS}} -P(m) \log P_\theta(m) - P(M_i^{OS}) \log P_\theta(M_i^{OS}) \quad (8)$$

In cases where $P(M_i^{OS}) > 0$, perfectly optimizing $\mathcal{L}_{MLL}(\theta)$ yields predictions that have (incorrectly) redistributed $P(M_i^{OS})$ to other peaks. This undesirable behaviour can be avoided by minimizing $\mathcal{L}(\theta)$ instead.

4.6 Latent Entropy Regularization

Entropy is a useful tool for interpreting the model’s latent distributions. $H_\theta(N)$ quantifies the diversity of fragments that contribute to the spectrum; $H_\theta(F|n)$ describes variability in molecular formulae (hydrogen counts) for each fragment; $H_\theta(N|f)$ describes variability in fragment annotations for each predicted formula. For each latent variable $Z \in \{N, F, F|n, N|f\}$, we define a normalized entropy $\hat{H}(Z) = H(Z)/\log(|Z|)$. Normalization corrects for differences in support size, facilitating direct comparison of latent entropies across molecules of different sizes. Since entropy is differentiable, normalized latent entropy and prediction error can be jointly optimized using gradient-based methods. Incorporating normalized entropy into the objective function, as demonstrated in Equation 9, effectively imposes entropy regularization on the latent distributions.

Table 1: Spectrum Prediction Performance on the NIST20 MS/MS Dataset. C_{BIN} is binned cosine similarity (0.01 Da bins), C_{HUN} is the Hungarian cosine similarity (10 ppm tolerance). As NEIMS, MassFormer, and ICEBERG have binned outputs, they cannot be scored with C_{HUN} . Means and standard deviations are reported for 5 random seeds, with best scores in bold.

Model	InChIKey		Scaffold	
	$C_{\text{BIN}} \uparrow$	$C_{\text{HUN}} \uparrow$	$C_{\text{BIN}} \uparrow$	$C_{\text{HUN}} \uparrow$
FraGNNNet-D4	0.736 ± 0.002	0.709 ± 0.002	0.678 ± 0.005	0.654 ± 0.006
FraGNNNet-D3	0.721 ± 0.002	0.693 ± 0.002	0.659 ± 0.001	0.633 ± 0.001
GrAFF-MS	0.596 ± 0.005	0.602 ± 0.004	0.520 ± 0.005	0.518 ± 0.004
ICEBERG	0.707 ± 0.001	-	0.636 ± 0.002	-
MassFormer	0.639 ± 0.002	-	0.562 ± 0.003	-
NEIMS	0.635 ± 0.001	-	0.546 ± 0.003	-
Precursor-Only	0.319 ± 0.000	0.285 ± 0.000	0.313 ± 0.000	0.280 ± 0.000

$$\mathcal{L}_{\text{REG}}(\theta) = \mathcal{L}(\theta) + \alpha_N \hat{H}_\theta(N) + \alpha_F \hat{H}_\theta(F) + \alpha_{F|n} \hat{H}_\theta(F|n) + \alpha_{N|f} \hat{H}_\theta(N|f) \quad (9)$$

The tunable hyperparameters $a_Z \in \{\alpha_N, \alpha_F, \alpha_{F|n}, \alpha_{N|f}\}$ control the influence of the entropy regularizers. Since $\mathcal{L}_{\text{REG}}(\theta)$ is minimized, setting $\alpha_Z < 0$ will maximize the corresponding normalized entropy $\hat{H}_\theta(Z)$, and vice versa. Entropy regularization can be useful when assessing consistency of fragment annotations, as demonstrated in Section 5.4.

5 Experiments

5.1 Spectrum Prediction (C2MS)

We evaluated C2MS performance on a held-out portion of the NIST20 MS/MS dataset (Appendix A.9), comparing FraGNNNet with other binned and structured prediction models from the literature. ICEBERG (Goldman et al., 2024) is a structured C2MS approach that uses neural networks to generate molecule fragments and map them to a predicted spectrum. GrAFF-MS (Murphy et al., 2023) is a structured approach that predicts a distribution over a static library of common chemical formulae. MassFormer (Young et al., 2023) and NEIMS (Wei et al., 2019) are both binned approaches: the former uses a pretrained graph transformer model (Ying et al., 2021) to encode the molecule, while the latter relies on domain-specific chemical fingerprint representations (Rogers & Hahn, 2010). Precursor-Only is a trivial baseline that only predicts a peak centered on the mass of the precursor formula. For more details on the baseline models, refer to Appendix A.14.

The results are summarized in Table 1. FraGNNNet-D4, a version of our model that uses a $d = 4$ approximation of the fragmentation DAG, clearly outperformed other models in terms of cosine similarity. Increasing fragmentation depth from $d = 3$ (FraGNNNet-D3) had a positive impact on performance, as expected.

5.2 Compound Retrieval (MS2C)

Each model was also evaluated in a retrieval-based MS2C task. Our setup is similar to previous works (Goldman et al., 2024; Murphy et al., 2023): for each molecule X_i and associated MS/MS spectrum Y_i in the test set ($\approx 4,000$ pairs, Appendix A.9) a candidate set \mathcal{C}_i is constructed from X_i and 49 other molecules sampled from PubChem (Kim et al., 2019). Each $C_i \in \mathcal{C}_i - \{X_i\}$ is selected to have high chemical similarity with X_i as measured by Tanimoto similarity between chemical fingerprints (Rogers & Hahn, 2010). The C2MS models are tasked with predicting a set of spectra \hat{Y}_i for molecules $C_i \in \mathcal{C}_i$. The spectra \hat{Y}_i are ranked by their cosine similarity with the real spectrum Y_i , inducing a ranking on the molecules C_i . The models are scored based on their ability to correctly rank X_i in the Top- k . On the Scaffold split, FraGNNNet-D4

outperformed all baseline models for all values of k (Figure 4a), and its rank distribution was more skewed towards lower values of k (Figure 4b). A similar analysis on the InChIKey split is presented in Figure 7 in the Appendix.

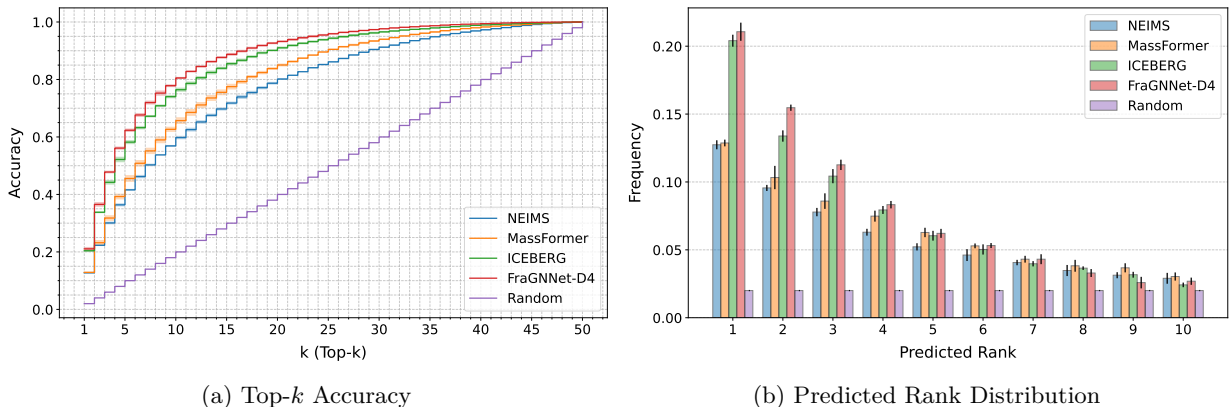


Figure 4: Compound retrieval results on the Scaffold split: Top- k Accuracy (a) for all values of $1 \leq k \leq 50$ and Predicted Rank Distribution (b) over ranks 1-10. Average over 5 seeds is reported; error bars indicate standard deviation.

5.3 Formula Annotations

Peak annotations (Section 2) are an important tool in the interpretation of MS/MS spectra. The FraGNNet model can produce both formula and fragment peak annotations (Figure 3 is an example). In this section we assess the quality of FraGNNet’s formula annotations, and in Section 5.4 we evaluate its fragment annotations.

The NIST20 dataset provides expert-curated formula annotations for most spectra; for more details on these annotations, refer to Appendix A.15. We formulate the formula annotation task as a classification problem. Given a real spectrum $P(m)$, each real peak $m \in M$ has a (possibly empty) set of associated expert formula annotations $A(m) = \{f_m^i\}_i$ that are assumed to be correct. Similarly, in the predicted spectrum $P_\theta(m')$ each predicted peak $m' \in M'$ has a (nonempty) set of associated formula annotations $A(m') = \{f_{m'}^i\}_i$.

Using a relative mass tolerance of 10 ppm, we match peaks in the predicted spectrum m' with peaks in the real spectrum m and identify overlap in their associated formula annotation sets $A(m')$ and $A(m)$. This allows us to calculate recall of annotated peaks in the real spectrum (Equation 27) and precision of annotated peaks in the predicted spectrum (Equation 29), as well as their intensity-weighted counterparts (Equations 28 and 30) and associated F_1 scores (Equations 31 and 32).

The results are summarized in Table 2. FraGNNet provided the best balance of recall and precision, as indicated by superior F_1 scores. GrAFF-MS achieved slightly higher recall and much lower precision; ICEBERG offered slightly higher precision but lower recall. GrAFF-MS relied on a static formula library, which yielded a distribution over roughly 10,000 formulae for each input compound. By comparison, FraGNNet’s formula distribution was typically much smaller, with a median support size of 679 formulae (Table 3). Note that GrAFF-MS directly used NIST formula annotations to define its formula library (refer to Appendix A.14.2 for full details); in contrast, the other models did not rely on expert annotations for training or inference.

5.4 Ensembling and Fragment Annotations

Fragment annotations provide greater model interpretability than formula annotations. FraGNNet’s latent distribution $P_\theta(n|f)$ naturally provides a map from formulae f to DAG nodes n and their associated fragments G_n . $P_\theta(n|f)$ can be interpreted as a fragment annotation distribution, indicating the likelihood of fragment G_n contributing to a peak centered around mass(f) (see Figure 3 for an example). However, the ground truth distribution $P(n|f)$ is generally unknown and difficult to measure experimentally. In principle, it is

Table 2: Formula Annotations (Scaffold Split). AR is Annotation Recall, AWR is Annotation Weighted Recall, AP is Annotation Precision, AWP is Annotation Weighted Precision, AF is Annotation F_1 score, AWF1 is Annotation Weighted F_1 score. Means and standard deviations (where applicable) are reported for 5 random seeds, with best scores in bold.

Model	AR \uparrow	AWR \uparrow	AP \uparrow	AWP \uparrow	AF1 \uparrow	AWF1 \uparrow
FraGNNNet-D4	0.81	0.90	0.98	1.00 \pm 0.00	0.89	0.95 \pm 0.00
GrAFF-MS	0.95	0.98	0.61	0.81 \pm 0.01	0.74	0.88 \pm 0.01
ICEBERG	0.66 \pm 0.00	0.81 \pm 0.00	0.99 \pm 0.00	-	0.79 \pm 0.00	-

possible for multiple fragments (with the same molecular formula) to contribute to the same peak, meaning that the true $P(n|f)$ is not necessarily degenerate.

Unlike the experiments in the previous section, there are no expert-curated fragment annotations that can be used for comparison. Rather than measuring the accuracy of the model annotations, we focus instead on measuring their consistency. In particular, we attempt to construct models with different fragment distributions that nonetheless achieve comparable spectrum prediction performance. Disagreement in fragment annotations between models that perform equally well would indicate that the model explanations are variable and therefore unreliable.

To achieve this, we construct four FraGNNNet-D4 ensembles, each with a different annotation distribution, by tuning the latent entropy regularization parameters (Section 4.6). The *Baseline Entropy* configuration represents a standard ensemble of K models without entropy regularization ($\alpha_{N|f} = 0$). The *High Entropy* and *Low Entropy* configurations consists of K models with entropy regularization ($\alpha_{N|f} < 0$ and $\alpha_{N|f} > 0$, respectively). The *Mixed Entropy* configuration consists of $K/3$ models each of the Baseline, Low, and High Entropy configurations. Except for the entropy regularization weights, all ensembles use the same hyperparameters and $K = 15$ different random seeds for initialization and training.

Let $\{\theta^k : \theta^k \sim P(\theta)\}_{k=1}^K$ denote the set of parameters for an ensemble of K models. We perform ensembling in the latent space (see Appendix A.16 for details). Let $P^K(n|f)$ and $\hat{H}^K(N|f)$ denote the latent distribution and latent normalized entropy (respectively) of a ensemble of K models. For each configuration, Figure 5a compares the behaviour of the individual models to the overall ensemble, in both the output space and the latent space. Ensembling provided a modest increase in cosine similarity (4.2 – 4.3%) and a somewhat larger increase in normalized entropy (7.6 – 11.4%). The observed entropy increases are consistent with theory; for a short proof see Appendix A.16.

Focusing now on the ensemble metrics, we can see that all four model configurations achieved similar MS/MS spectrum prediction performance ($C_{\text{HUN}} \approx 0.67$) despite differing markedly in normalized entropy: the Low Entropy configuration only had $\approx 71\%$ of the normalized entropy of the High Entropy configuration (0.37 vs 0.52, respectively). This confirms FraGNNNet models with different fragment annotation distributions can achieve similar C2MS performance.

Viewed in isolation, these results might suggest that FraGNNNet’s fragment annotations are inconsistent and raise questions about their reliability. However, we also investigated the top-1 fragment agreement (*i.e.*, $P^K(n|f)$ mode consistency) between ensemble configurations. This behaviour was measured using pairwise fragment annotation agreement (PFA, Equation 38) and consensus fragment annotation agreement (CFA, Equation 39). In the NIST20 MS/MS test set, $\text{PFA} \geq 82\%$ (Figure 5b) and $\text{CFA} \approx 76\%$ across all model configurations. These results demonstrate that the modes of the annotation distributions $P_\theta(n|f)$ were relatively consistent and robust to variations in latent entropy. In Appendix A.17 we performed a similar analysis focusing on $P_\theta(\tilde{n}|f)$, the version of the annotation distribution that accounts for fragment isomorphism (Appendix A.3). In this case the top-1 agreement was even higher ($\text{PFA} \geq 91\%$, $\text{CFA} \approx 89\%$ consensus).

In summary, we have shown that it is possible to achieve comparable performance with ensembles that differ significantly in their normalized latent entropies $H_\theta^K(N|f)$. However, despite these entropy differences, the

models tend to agree on which fragment annotation G_n is most appropriate for a given formula f and its associated peak at $\text{mass}(f)$. Although we cannot establish the true fragment annotations without specialized measurements (van Tetering et al., 2024), our experiments indicate that the FraGNNet’s explanations remain robust to perturbations in latent entropy, which is critical for ensuring reliability.

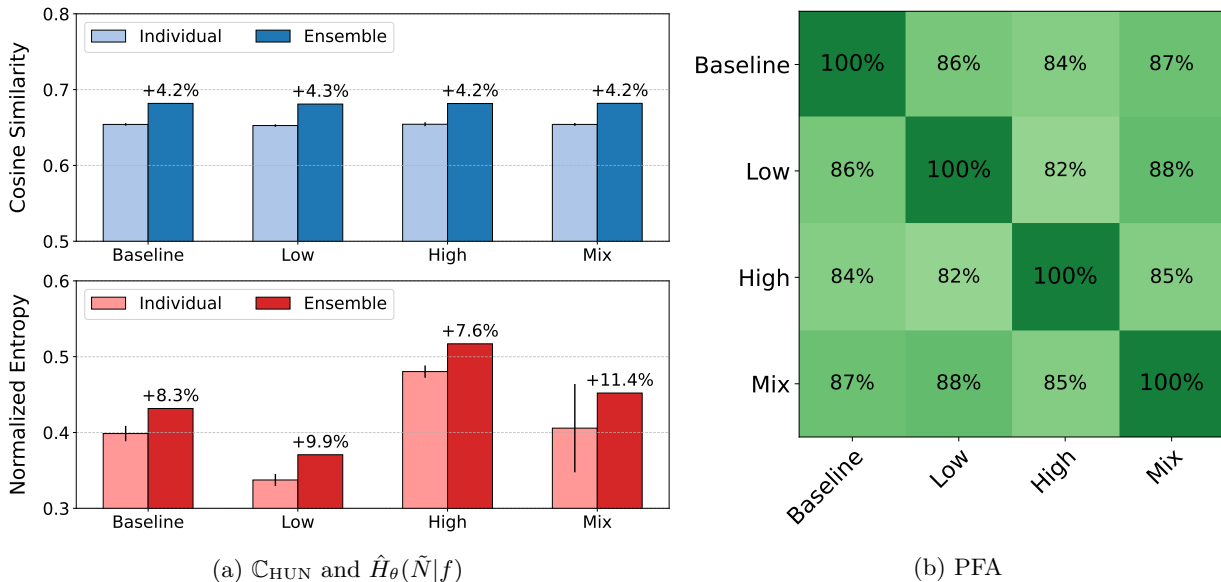


Figure 5: (a) For each ensemble configuration (Baseline, Low, High, Mix), the cosine similarity \mathbb{C}_{HUN} and normalized entropy of the annotation distribution $\hat{H}_{\theta}(\tilde{N}|f)$ are reported. For both metrics, the average score of the individual models (Individual) is compared with the score of the ensemble (Ensemble). Each ensemble consists of $K = 15$ models. Standard deviations for the K individual models are plotted as error bars. (b) Pairwise fragment annotation agreement (PFA) for all ensemble combinations are plotted in a matrix. The consensus agreement (CFA) is $\approx 76\%$.

6 Discussion

In this work we introduce FraGNNet, a deep probabilistic model for spectrum prediction. Our work shows that pairing combinatorial fragmentation with graph neural networks can achieve state-of-the-art C2MS performance. FraGNNet is unique in its interpretable probabilistic representation of fragmentation. Features such as OS prediction and tunable entropy regularization further differentiate it from existing models. Strong results in compound retrieval and peak annotation demonstrate potential utility in MS2C applications.

Several avenues exist to enhance our method. First, the fragmentation algorithm currently depends on recursive edge-removal operations, which could be parallelized to accelerate runtime. Second, the algorithm fails to account for some fragments, as evidenced by unexplained OS peaks in the spectra. These peaks may arise from complex chemistry, such as cyclizations, that dramatically expand the fragment search space and are therefore challenging to model. One potential remedy is to develop a sequential reaction sampler that can generate fragments beyond simple bond-breaking. Alternatively, combining FraGNNet with a more flexible C2MS model, such as a formula predictor like GrAFF-MS, could be an effective method of capturing OS peaks without explicitly modelling their fragments. Finally, to broaden FraGNNet’s practical utility, it is important to evaluate performance on unmerged spectra and under a broader range of experimental conditions, including different instrument platforms and precursor adducts.

References

- Felicity Allen, Russell Greiner, and David Wishart. Competitive fragmentation modeling of ESI-MS/MS spectra for putative metabolite identification. *Metabolomics*, 11(1):98–110, February 2015. ISSN 1573-3890. doi: 10.1007/s11306-014-0676-4. URL <https://doi.org/10.1007/s11306-014-0676-4>.
- Peter W. Battaglia, Jessica B. Hamrick, Victor Bapst, Alvaro Sanchez-Gonzalez, Vinicius Zambaldi, Mateusz Malinowski, Andrea Tacchetti, David Raposo, Adam Santoro, Ryan Faulkner, Caglar Gulcehre, Francis Song, Andrew Ballard, Justin Gilmer, George Dahl, Ashish Vaswani, Kelsey Allen, Charles Nash, Victoria Langston, Chris Dyer, Nicolas Heess, Daan Wierstra, Pushmeet Kohli, Matt Botvinick, Oriol Vinyals, Yujia Li, and Razvan Pascanu. Relational inductive biases, deep learning, and graph networks. *arXiv:1806.01261 [cs, stat]*, October 2018. URL <http://arxiv.org/abs/1806.01261>.
- Stefan Behnel, Robert Bradshaw, Craig Citro, Lisandro Dalcin, Dag Sverre Seljebotn, and Kurt Smith. Cython: The best of both worlds. *Computing in Science & Engineering*, 13(2):31–39, 2011.
- Guy W. Bemis and Mark A. Murcko. The Properties of Known Drugs. 1. Molecular Frameworks. *Journal of Medicinal Chemistry*, 39(15):2887–2893, January 1996. ISSN 0022-2623. doi: 10.1021/jm9602928. URL <https://doi.org/10.1021/jm9602928>.
- Lukas Biewald. Experiment tracking with weights and biases, 2020. URL <https://www.wandb.com/>. Software available from wandb.com.
- Montgomery Bohde, Mrunali Manjrekar, Runzhong Wang, Shuiwang Ji, and Connor W. Coley. DiffMS: Diffusion Generation of Molecules Conditioned on Mass Spectra, February 2025. URL <http://arxiv.org/abs/2502.09571>. arXiv:2502.09571 [cs].
- Roman Bushuiev, Anton Bushuiev, Niek F. de Jonge, Adamo Young, Fleming Kretschmer, Raman Samusevich, Janne Heirman, Fei Wang, Luke Zhang, Kai Dührkop, Marcus Ludwig, Nils A. Haupt, Apurva Kalia, Corinna Brungs, Robin Schmid, Russell Greiner, BO WANG, David Wishart, Liping Liu, Juho Rousu, Wout Bittremieux, Hannes Rost, Tytus D. Mak, Soha Hassoun, Florian Huber, Justin J.J. van der Hooft, Michael A. Stravs, Sebastian Böcker, Josef Sivic, and Tomas Pluskal. Massspecgym: A benchmark for the discovery and identification of molecules. In *The Thirty-eight Conference on Neural Information Processing Systems Datasets and Benchmarks Track*, 2024. URL <https://openreview.net/forum?id=AAo8zAShX3>.
- Roman Bushuiev, Anton Bushuiev, Raman Samusevich, Corinna Brungs, Josef Sivic, and Tomáš Pluskal. Emergence of molecular structures from repository-scale self-supervised learning on tandem mass spectra, January 2025. URL <https://chemrxiv.org/engage/chemrxiv/article-details/678bfa1c6dde43c90815ccc5>.
- Thomas Butler, Abraham Frandsen, Rose Lightheart, Brian Bargh, James Taylor, T. J. Bollerman, Thomas Kerby, Kiana West, Gennady Voronov, Kevin Moon, Tobias Kind, Pieter Dorrestein, August Allen, Viswa Colluru, and David Healey. MS2mol: A transformer model for illuminating dark chemical space from mass spectra, 2023. URL <https://chemrxiv.org/engage/chemrxiv/article-details/6492507524989702c2b082fc>.
- Maria Emilia Dueñas, Rachel E Peltier-Heap, Melanie Leveridge, Roland S Annan, Frank H Büttner, and Matthias Trost. Advances in high-throughput mass spectrometry in drug discovery. *EMBO Molecular Medicine*, 15(1):e14850, December 2022. ISSN 1757-4676. doi: 10.15252/emmm.202114850. URL <https://www.ncbi.nlm.nih.gov/pmc/articles/PMC9832828/>.
- Kai Dührkop, Huibin Shen, Marvin Meusel, Juho Rousu, and Sebastian Böcker. Searching molecular structure databases with tandem mass spectra using csi:fingerid. *Proceedings of the National Academy of Sciences*, 112(41):12580–12585, 2015. ISSN 0027-8424. doi: 10.1073/pnas.1509788112. URL <https://www.pnas.org/content/112/41/12580>.
- Joseph L. Durant, Burton A. Leland, Douglas R. Henry, and James G. Nourse. Reoptimization of MDL keys for use in drug discovery. *Journal of Chemical Information and Computer Sciences*, 42(6):1273–1280, 2002. ISSN 0095-2338. doi: 10.1021/ci010132r.

- Kai Dührkop, Markus Fleischauer, Marcus Ludwig, Alexander A. Aksenov, Alexey V. Melnik, Marvin Meusel, Pieter C. Dorrestein, Juho Rousu, and Sebastian Böcker. SIRIUS 4: a rapid tool for turning tandem mass spectra into metabolite structure information. *Nature Methods*, 16(4):299–302, April 2019. ISSN 1548-7105. doi: 10.1038/s41592-019-0344-8. URL <http://www.nature.com/articles/s41592-019-0344-8>.
- William Falcon and The PyTorch Lightning team. PyTorch Lightning, March 2019. URL <https://github.com/Lightning-AI/lightning>.
- Matthias Fey and Jan Eric Lenssen. Fast graph representation learning with pytorch geometric. *CoRR*, abs/1903.02428, 2019. URL <http://arxiv.org/abs/1903.02428>.
- Samuel Goldman, John Bradshaw, Jiayi Xin, and Connor Coley. Prefix-Tree Decoding for Predicting Mass Spectra from Molecules. In A. Oh, T. Neumann, A. Globerson, K. Saenko, M. Hardt, and S. Levine (eds.), *Advances in Neural Information Processing Systems*, volume 36, pp. 48548–48572. Curran Associates, Inc., 2023a. URL https://proceedings.neurips.cc/paper_files/paper/2023/file/97d596ca21d0751ba2c633bad696cf7f-Paper-Conference.pdf.
- Samuel Goldman, Jeremy Wohlwend, Martin Stražar, Guy Haroush, Ramnik J. Xavier, and Connor W. Coley. Annotating metabolite mass spectra with domain-inspired chemical formula transformers. *Nature Machine Intelligence*, 5(9):965–979, 2023b. ISSN 2522-5839. doi: 10.1038/s42256-023-00708-3. URL <https://www.nature.com/articles/s42256-023-00708-3>. Number: 9 Publisher: Nature Publishing Group.
- Samuel Goldman, Jiayi Xin, Joules Provenzano, and Connor W. Coley. MIST-CF: Chemical Formula Inference from Tandem Mass Spectra. *Journal of Chemical Information and Modeling*, September 2023c. ISSN 1549-9596. doi: 10.1021/acs.jcim.3c01082. URL <https://doi.org/10.1021/acs.jcim.3c01082>. Publisher: American Chemical Society.
- Samuel Goldman, Janet Li, and Connor W. Coley. Generating Molecular Fragmentation Graphs with Autoregressive Neural Networks. *Analytical Chemistry*, 96(8):3419–3428, February 2024. ISSN 0003-2700. doi: 10.1021/acs.analchem.3c04654. URL <https://doi.org/10.1021/acs.analchem.3c04654>. Publisher: American Chemical Society.
- G.A. Nagana Gowda and Danijel Djukovic. Overview of Mass Spectrometry-Based Metabolomics: Opportunities and Challenges. *Methods in molecular biology (Clifton, N.J.)*, 1198:3–12, 2014. ISSN 1064-3745. doi: 10.1007/978-1-4939-1258-2_1. URL <https://www.ncbi.nlm.nih.gov/pmc/articles/PMC4336784/>.
- Aric Hagberg, Pieter Swart, and Daniel S Chult. Exploring network structure, dynamics, and function using networkx. Technical report, Los Alamos National Lab.(LANL), Los Alamos, NM (United States), 2008.
- Stephen R. Heller, Alan McNaught, Igor Pletnev, Stephen Stein, and Dmitrii Tchekhovskoi. InChI, the IUPAC International Chemical Identifier. *Journal of Cheminformatics*, 7(1):23, May 2015. ISSN 1758-2946. doi: 10.1186/s13321-015-0068-4. URL <https://doi.org/10.1186/s13321-015-0068-4>.
- Yuhui Hong, Sujun Li, Christopher J Welch, Shane Tichy, Yuzhen Ye, and Haixu Tang. 3DMolMS: prediction of tandem mass spectra from 3D molecular conformations. *Bioinformatics*, 39(6):btad354, May 2023. ISSN 1367-4811. doi: 10.1093/bioinformatics/btad354. URL <https://doi.org/10.1093/bioinformatics/btad354>. _eprint: <https://academic.oup.com/bioinformatics/article-pdf/39/6/btad354/50661428/btad354.pdf>.
- Florian Huber, Stefan Verhoeven, Christiaan Meijer, Hanno Spreeuw, Efraín Manuel Villanueva Castilla, Cunliang Geng, Justin J. j van der Hooft, Simon Rogers, Adam Belloum, Faruk Diblen, and Jurriaan H. Spaaks. matchms - processing and similarity evaluation of mass spectrometry data. *Journal of Open Source Software*, 5(52):2411, August 2020. ISSN 2475-9066. doi: 10.21105/joss.02411. URL <https://joss.theoj.org/papers/10.21105/joss.02411>.
- Andrew R. Johnson and Erin E. Carlson. Collision-induced dissociation mass spectrometry: A powerful tool for natural product structure elucidation. *Analytical Chemistry*, 87(21):10668–10678, November 2015. ISSN 0003-2700, 1520-6882. doi: 10.1021/acs.analchem.5b01543.

- Sunghwan Kim, Jie Chen, Tiejun Cheng, Asta Gindulyte, Jia He, Siqian He, Qingliang Li, Benjamin A Shoemaker, Paul A Thiessen, Bo Yu, Leonid Zaslavsky, Jian Zhang, and Evan E Bolton. PubChem 2019 update: improved access to chemical data. *Nucleic Acids Research*, 47(Database issue):D1102–D1109, January 2019. ISSN 0305-1048. doi: 10.1093/nar/gky1033. URL <https://www.ncbi.nlm.nih.gov/pmc/articles/PMC6324075/>.
- Tobias Kind, Hiroshi Tsugawa, Tomas Cajka, Yan Ma, Zijuan Lai, Sajjan S. Mehta, Gert Wohlgemuth, Dinesh Kumar Barupal, Megan R. Showalter, Masanori Arita, and Oliver Fiehn. Identification of small molecules using accurate mass MS/MS search. *Mass spectrometry reviews*, 37(4):513–532, July 2018. ISSN 0277-7037. doi: 10.1002/mas.21535. URL <https://www.ncbi.nlm.nih.gov/pmc/articles/PMC8106966/>.
- Kezhi Kong, Guohao Li, Mucong Ding, Zuxuan Wu, Chen Zhu, Bernard Ghanem, Gavin Taylor, and Tom Goldstein. Robust optimization as data augmentation for large-scale graphs. In *Proceedings of the IEEE/CVF Conference on Computer Vision and Pattern Recognition*, pp. 60–69, 2022.
- H. W. Kuhn. The Hungarian method for the assignment problem. *Naval Research Logistics Quarterly*, 2(1-2):83–97, March 1955. ISSN 0028-1441, 1931-9193. doi: 10.1002/nav.3800020109. URL <https://onlinelibrary.wiley.com/doi/10.1002/nav.3800020109>.
- Greg Landrum. Rdkit: Open-source cheminformatics, 2022. URL <http://www.rdkit.org>.
- Albert T. Lebedev. Environmental Mass Spectrometry. *Annual Review of Analytical Chemistry*, 6(1):163–189, 2013. doi: 10.1146/annurev-anchem-062012-092604. URL <https://doi.org/10.1146/annurev-anchem-062012-092604>.
- Xinmeng Li, Hao Zhu, Li-ping Liu, and Soha Hassoun. Ensemble Spectral Prediction (ESP) Model for Metabolite Annotation. *arXiv:2203.13783 [cs, q-bio]*, March 2022. URL <http://arxiv.org/abs/2203.13783>. arXiv: 2203.13783.
- Michael Murphy, Stefanie Jegelka, Ernest Fraenkel, Tobias Kind, David Healey, and Thomas Butler. Efficiently predicting high resolution mass spectra with graph neural networks. In Andreas Krause, Emma Brunskill, Kyunghyun Cho, Barbara Engelhardt, Sivan Sabato, and Jonathan Scarlett (eds.), *Proceedings of the 40th International Conference on Machine Learning*, volume 202 of *Proceedings of Machine Learning Research*, pp. 25549–25562. PMLR, July 2023. URL <https://proceedings.mlr.press/v202/murphy23a.html>.
- Maho Nakata and Tomomi Shimazaki. PubChemQC Project: A Large-Scale First-Principles Electronic Structure Database for Data-Driven Chemistry. *Journal of Chemical Information and Modeling*, 57(6): 1300–1308, June 2017. ISSN 1549-9596. doi: 10.1021/acs.jcim.7b00083. URL <https://doi.org/10.1021/acs.jcim.7b00083>.
- Yannek Nowatzky, Francesco Friedrich Russo, Jan Lisec, Alexander Kister, Knut Reinert, Thilo Muth, and Philipp Benner. FIORA: Local neighborhood-based prediction of compound mass spectra from single fragmentation events. *Nature Communications*, 16(1):2298, March 2025. ISSN 2041-1723. doi: 10.1038/s41467-025-57422-4. URL <https://www.nature.com/articles/s41467-025-57422-4>. Publisher: Nature Publishing Group.
- Jiwon Park, Jeonghee Jo, and Sungroh Yoon. Mass spectra prediction with structural motif-based graph neural networks. *Scientific Reports*, 14(1):1400, January 2024. ISSN 2045-2322. doi: 10.1038/s41598-024-51760-x. URL <https://www.nature.com/articles/s41598-024-51760-x>. Publisher: Nature Publishing Group.
- Adam Paszke, Sam Gross, Francisco Massa, Adam Lerer, James Bradbury, Gregory Chanan, Trevor Killeen, Zeming Lin, Natalia Gimelshein, Luca Antiga, Alban Desmaison, Andreas Köpf, Edward Yang, Zach DeVito, Martin Raison, Alykhan Tejani, Sasank Chilamkurthy, Benoit Steiner, Lu Fang, Junjie Bai, and Soumith Chintala. PyTorch: An Imperative Style, High-Performance Deep Learning Library. *arXiv:1912.01703 [cs, stat]*, December 2019. URL <http://arxiv.org/abs/1912.01703>.
- Frank T. Peters. Recent advances of liquid chromatography–(tandem) mass spectrometry in clinical and forensic toxicology. *Clinical Biochemistry*, 44(1):54–65, January 2011. ISSN 0009-9120. doi: 10.1016/j.clin

- biochem.2010.08.008. URL <https://www.sciencedirect.com/science/article/pii/S0009912010003486>.
- Python Core Team. *Python: A dynamic, open source programming language*. Python Software Foundation, 2021. URL <https://www.python.org/>.
- Hantao Qiang, Fei Wang, Wenyun Lu, Xi Xing, Hahn Kim, Sandrine A.M. Merette, Lucas B. Ayres, Eponine Oler, Jenna E. AbuSalim, Asael Roichman, Michael Neinast, Ricardo A. Cordova, Won Dong Lee, Ehud Herbst, Vishu Gupta, Samuel Neff, Mickel Hiebert-Giesbrecht, Adamo Young, Vasuk Gautam, Siyang Tian, Bo Wang, Hannes Röst, Russell Greiner, Li Chen, Chad W. Johnston, Leonard J. Foster, Aaron M. Shapiro, David S. Wishart, Joshua D. Rabinowitz, and Michael A. Skinnider. Language model-guided anticipation and discovery of unknown metabolites. *bioRxiv*, 2024. doi: 10.1101/2024.11.13.623458. URL <https://www.biorxiv.org/content/early/2024/11/15/2024.11.13.623458>.
- Lars Ridder, Justin J. J. van der Hooft, and Stefan Verhoeven. Automatic Compound Annotation from Mass Spectrometry Data Using MAGMa. *Mass Spectrometry*, 3(Special_Issue_2):S0033–S0033, 2014. doi: 10.5702/massspectrometry.S0033.
- David Rogers and Mathew Hahn. Extended-Connectivity Fingerprints. *Journal of Chemical Information and Modeling*, 50(5):742–754, May 2010. ISSN 1549-9596. doi: 10.1021/ci100050t. URL <https://doi.org/10.1021/ci100050t>.
- Christoph Ruttkies, Emma L. Schymanski, Sebastian Wolf, Juliane Hollender, and Steffen Neumann. MetFrag relaunched: incorporating strategies beyond in silico fragmentation. *Journal of Cheminformatics*, 8(1):3, January 2016. ISSN 1758-2946. doi: 10.1186/s13321-016-0115-9. URL <https://doi.org/10.1186/s13321-016-0115-9>.
- Emma L. Schymanski, Christoph Ruttkies, Martin Krauss, Céline Brouard, Tobias Kind, Kai Dührkop, Felicity Allen, Arpana Vaniya, Dries Verdegem, Sebastian Böcker, Juho Rousu, Huibin Shen, Hiroshi Tsugawa, Tanvir Sajed, Oliver Fiehn, Bart Ghesquière, and Steffen Neumann. Critical Assessment of Small Molecule Identification 2016: automated methods. *Journal of Cheminformatics*, 9(1):22, March 2017. ISSN 1758-2946. doi: 10.1186/s13321-017-0207-1. URL <https://doi.org/10.1186/s13321-017-0207-1>.
- Nino Shervashidze, Pascal Schweitzer, Erik Jan van Leeuwen, Kurt Mehlhorn, and Karsten M. Borgwardt. Weisfeiler-Lehman Graph Kernels. *Journal of Machine Learning Research*, 12(77):2539–2561, 2011. URL <http://jmlr.org/papers/v12/shervashidze11a.html>.
- Aditya Divyakant Shrivastava, Neil Swainston, Soumitra Samanta, Ivayla Roberts, Marina Wright Muelas, and Douglas B. Kell. MassGenie: A Transformer-Based Deep Learning Method for Identifying Small Molecules from Their Mass Spectra. *Biomolecules*, 11(12):1793, November 2021. ISSN 2218-273X. doi: 10.3390/biom11121793. URL <https://www.ncbi.nlm.nih.gov/pmc/articles/PMC8699281/>.
- Michael A. Skinnider, Fei Wang, Daniel Pasin, Russell Greiner, Leonard J. Foster, Petur W. Dalsgaard, and David S. Wishart. A deep generative model enables automated structure elucidation of novel psychoactive substances. *Nature Machine Intelligence*, 3(11):973–984, November 2021. ISSN 2522-5839. doi: 10.1038/s42256-021-00407-x. URL <https://www.nature.com/articles/s42256-021-00407-x>. Number: 11 Publisher: Nature Publishing Group.
- Arnold Steckel and Gitta Schlosser. An organic chemist’s guide to electrospray mass spectrometric structure elucidation. *Molecules*, 24(3):611, February 2019. ISSN 1420-3049. doi: 10.3390/molecules24030611.
- Stephen Stein. Mass Spectral Reference Libraries: An Ever-Expanding Resource for Chemical Identification. *Analytical Chemistry*, 84(17):7274–7282, September 2012. ISSN 0003-2700. doi: 10.1021/ac301205z. URL <https://doi.org/10.1021/ac301205z>.
- Stephen Stein. NIST/EPA/NIH Mass spectral library with search program data version: NIST v23, 2023.

- Stephen E. Stein and Donald R. Scott. Optimization and testing of mass spectral library search algorithms for compound identification. *Journal of the American Society for Mass Spectrometry*, 5(9):859–866, September 1994. ISSN 1044-0305. doi: 10.1016/1044-0305(94)87009-8. URL <https://pubs.acs.org/doi/10.1016/1044-0305%2894%2987009-8>.
- Michael A. Stravs, Kai Dührkop, Sebastian Böcker, and Nicola Zamboni. MSNovelist: de novo structure generation from mass spectra. *Nature Methods*, 19(7):865–870, July 2022. ISSN 1548-7105. doi: 10.1038/s41592-022-01486-3. URL <https://www.nature.com/articles/s41592-022-01486-3>. Number: 7 Publisher: Nature Publishing Group.
- Matthew Tancik, Pratul P. Srinivasan, Ben Mildenhall, Sara Fridovich-Keil, Nithin Raghavan, Utkarsh Singhal, Ravi Ramamoorthi, Jonathan T. Barron, and Ren Ng. Fourier features let networks learn high frequency functions in low dimensional domains. *CoRR*, abs/2006.10739, 2020. URL <https://arxiv.org/abs/2006.10739>.
- Lara van Tetering, Sylvia Spies, Quirine D. K. Wildeman, Kas J. Houthuijs, Rianne E. van Outersterp, Jonathan Martens, Ron A. Wevers, David S. Wishart, Giel Berden, and Jos Oomens. A spectroscopic test suggests that fragment ion structure annotations in MS/MS libraries are frequently incorrect. *Communications Chemistry*, 7(1):1–11, February 2024. ISSN 2399-3669. doi: 10.1038/s42004-024-01112-7. URL <https://www.nature.com/articles/s42004-024-01112-7>. Number: 1 Publisher: Nature Publishing Group.
- Gennady Voronov, Abe Frandsen, Brian Bargh, David Healey, Rose Lightheart, Tobias Kind, Pieter Dorrestein, Viswa Colluru, and Thomas Butler. Ms2prop: A machine learning model that directly predicts chemical properties from mass spectrometry data for novel compounds. *bioRxiv*, 2022. doi: 10.1101/2022.10.09.511482. URL <https://www.biorxiv.org/content/early/2022/10/11/2022.10.09.511482>.
- Fei Wang, Jaanus Liigand, Siyang Tian, David Arndt, Russell Greiner, and David S. Wishart. CFM-ID 4.0: More Accurate ESI-MS/MS Spectral Prediction and Compound Identification. *Analytical Chemistry*, August 2021. ISSN 0003-2700. doi: 10.1021/acs.analchem.1c01465. URL <https://doi.org/10.1021/acs.analchem.1c01465>.
- Fei Wang, Daniel Pasin, Michael A. Skinnider, Jaanus Liigand, Jan-Niklas Kleis, David Brown, Eponine Oler, Tanvir Sajed, Vasuk Gautam, Stephen Harrison, Russell Greiner, Leonard J. Foster, Petur Weihe Dalsgaard, and David S. Wishart. Deep Learning-Enabled MS/MS Spectrum Prediction Facilitates Automated Identification Of Novel Psychoactive Substances. *Analytical Chemistry*, 95(50):18326–18334, December 2023. ISSN 0003-2700. doi: 10.1021/acs.analchem.3c02413. URL <https://doi.org/10.1021/acs.analchem.3c02413>. Publisher: American Chemical Society.
- Yinkai Wang, Xiaohui Chen, Liping Liu, and Soha Hassoun. Madgen: Mass-spec attends to de novo molecular generation, 2025. URL <https://arxiv.org/abs/2501.01950>.
- Jennifer N. Wei, David Belanger, Ryan P. Adams, and D. Sculley. Rapid prediction of electron-ionization mass spectrometry using neural networks. *ACS Central Science*, 5(4):700–708, April 2019. ISSN 2374-7943, 2374-7951. doi: 10.1021/acscentsci.9b00085. URL <https://pubs.acs.org/doi/10.1021/acscentsci.9b00085>.
- David S. Wishart, Yannick Djoumbou Feunang, Ana Marcu, An Chi Guo, Kevin Liang, Rosa Vázquez-Fresno, Tanvir Sajed, Daniel Johnson, Carin Li, Naama Karu, Zinat Sayeeda, Elvis Lo, Nazanin Assempour, Mark Berjanskii, Sandeep Singhal, David Arndt, Yonjie Liang, Hasan Badran, Jason Grant, Arnau Serra-Cayuela, Yifeng Liu, Rupa Mandal, Vanessa Neveu, Allison Pon, Craig Knox, Michael Wilson, Claudine Manach, and Augustin Scalbert. HMDB 4.0: the human metabolome database for 2018. *Nucleic Acids Research*, 46 (D1):D608–D617, January 2018. ISSN 1362-4962. doi: 10.1093/nar/gkx1089.
- Sebastian Wolf, Stephan Schmidt, Matthias Müller-Hannemann, and Steffen Neumann. In silico fragmentation for computer assisted identification of metabolite mass spectra. *BMC Bioinformatics*, 11(1):148, March 2010. ISSN 1471-2105. doi: 10.1186/1471-2105-11-148. URL <https://doi.org/10.1186/1471-2105-11-148>.

- Zhenqin Wu, Bharath Ramsundar, Evan N. Feinberg, Joseph Gomes, Caleb Geniesse, Aneesh S. Pappu, Karl Leswing, and Vijay Pande. MoleculeNet: a benchmark for molecular machine learning. *Chemical Science*, 9(2):513–530, January 2018. ISSN 2041-6539. doi: 10.1039/C7SC02664A. URL <https://pubs.rsc.org/en/content/articlelanding/2018/sc/c7sc02664a>. Publisher: The Royal Society of Chemistry.
- Keyulu Xu, Weihua Hu, Jure Leskovec, and Stefanie Jegelka. How powerful are graph neural networks? In *International Conference on Learning Representations*, 2019. URL <https://openreview.net/forum?id=ryGs6iA5Km>.
- Xiaoyu Yang, Pedatsur Neta, and Stephen E. Stein. Quality Control for Building Libraries from Electrospray Ionization Tandem Mass Spectra. *Analytical Chemistry*, 86(13):6393–6400, July 2014. ISSN 0003-2700, 1520-6882. doi: 10.1021/ac500711m. URL <https://pubs.acs.org/doi/10.1021/ac500711m>.
- Chengxuan Ying, Tianle Cai, Shengjie Luo, Shuxin Zheng, Guolin Ke, Di He, Yanming Shen, and Tie-Yan Liu. Do transformers really perform bad for graph representation? *Neural Information Processing Systems (NeurIPS)*, 2021.
- Adamo Young, Bo Wang, and Hannes Röst. MassFormer: Tandem Mass Spectrum Prediction for Small Molecules using Graph Transformers, May 2023. URL <http://arxiv.org/abs/2111.04824>. arXiv:2111.04824 [cs, q-bio].
- Hao Zhu, Liping Liu, and Soha Hassoun. Using Graph Neural Networks for Mass Spectrometry Prediction. *arXiv:2010.04661 [cs]*, October 2020. URL <http://arxiv.org/abs/2010.04661>.
- Richard Licheng Zhu and Eric Jonas. Rapid Approximate Subset-Based Spectra Prediction for Electron Ionization–Mass Spectrometry. *Analytical Chemistry*, 95(5):2653–2663, February 2023. ISSN 0003-2700. doi: 10.1021/acs.analchem.2c02093. URL <https://doi.org/10.1021/acs.analchem.2c02093>. Publisher: American Chemical Society.

A Appendix

A.1 Recursive Fragmentation Algorithm

Algorithm 1 RecFrag

Input: graph $G = (V, E)$, max depth d , current depth d'
 Initialize DAG nodes $V_F = \{\}$, DAG edges $E_F = \{\}$
if $d' \leq d$ **then**
 $S = \emptyset$
 $I = \text{ID}(V, E)$
 for $e = (u, v) \in E$ **do**
 $E' = E - \{e\}$
 $(V^u, E^u) = \text{BFSCC}(u, V, E')$
 $I^u = \text{ID}(V^u, E^u)$
 $(V^v, E^v) = \text{BFSCC}(v, V, E')$
 $I^v = \text{ID}(V^v, E^v)$
 $S = S \cup \{(V^u, E^u), (V^v, E^v)\}$
 $V_F = V_F \cup \{I^u, I^v\}$
 $E_F = E_F \cup \{(I, I^u), (I, I^v)\}$
 end for
 for $G^s = (V^s, E^s) \in S$ **do**
 $(V_F^s, E_F^s) = \text{RecFrag}(G^s, d, d' + 1)$
 $V_F = V_F \cup V_F^s$
 $E_F = E_F \cup E_F^s$
 end for
end if
 Return (V_F, E_F)

The approximate fragmentation DAG $G_{\mathcal{F}^d}$ is constructed by calling Algorithm 1 on the heavy-atom skeleton of the molecule $\mathcal{H}(G)$, with initial depth parameter $d' = 1$. BFSCC is a breadth-first search algorithm that returns the set of nodes and edges in a graph that can be reached from a given input node. We apply BFSCC to identify connected components (fragment subgraphs) of $\mathcal{H}(G)$ after each edge removal. ID is a function that maps every subgraph of $\mathcal{H}(G)$ to a unique integer id (our implementation just uses an enumeration).

We apply a post-processing step that merges fragments $n_1, n_2 \in V_F$ with the same atom sets $V^{n_1} = V^{n_2}$. These fragments arise when bond are removed from non-linear structures in the molecule, such as rings. The merging works as follows: the nodes $\{n_i\}_i$ in the DAG whose associated fragment subgraphs $\{G^{n_i}\}_i$ all have the same atom set V^n are removed from $G_{\mathcal{F}^d}$ and replaced with a new DAG node m that retains all edges of the removed nodes. The associated fragment subgraph $G^m = (V^m, E^m)$ is defined as the vertex-induced subgraph of V^n (Equations 10 and 11):

$$V^m = V^n \tag{10}$$

$$E^m = \{(u, v) \in E : u \in V^n \wedge v \in V^n\} \tag{11}$$

After post-processing, it is possible to assign each node n in the DAG a unique ID based only on its atom set V^n . Note that the DAG node merging can introduce self-edges in $G_{\mathcal{F}^d}$, implying that $G_{\mathcal{F}^d}$ is not always a true DAG in practice.

Figure 6 is a visualization of the full fragmentation DAG \mathcal{F}_G for an example molecule. Since this molecule is small and linear, the resulting DAG consists of only 10 nodes and 19 edges.

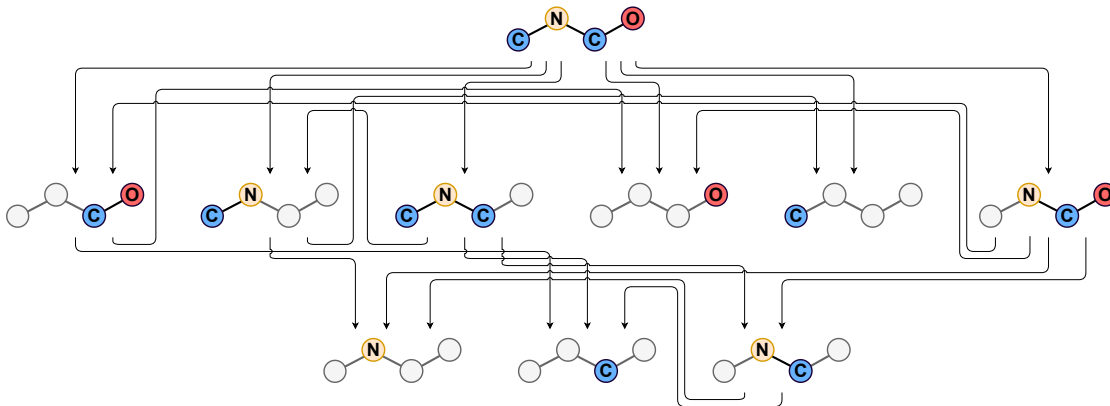


Figure 6: DAG Visualization: the approximate fragmentation DAG $\mathcal{G}_{\mathcal{F}^d}$ ($d = 3$) for a small molecule, methylaminomethanol. The root node is represented by the heavy-atom skeleton of the molecule $\mathcal{H}(G)$, and each other node is represented by a connected subgraph of $\mathcal{H}(G)$. Carbon atoms are represented by C, nitrogen atoms by N, oxygen atoms by O.

Table 3: Fragmentation DAG Statistics over the NIST20 MS/MS Dataset. PP is peak precision, PWP is peak weighted precision, PR is peak recall, PWR is peak weighted recall.

STATISTICS	D3 ($d = 3, j = 4$)					D4 ($d = 4, j = 4$)				
	MIN	25%	50%	75%	MAX	MIN	25%	50%	75%	MAX
# FORMULAE f	4	323	527	838	7239	4	388	679	1160	13146
# NODES n	10	167	280	474	5022	10	333	677	1392	32902
# NODES \tilde{n}	9	104	173	308	4518	9	183	379	865	31688
# EDGES e	20	662	1156	2138	44952	20	2288	4790	10020	249138
PR	0.00	0.51	0.64	0.77	1.00	0.00	0.63	0.75	0.85	1.00
PWR	0.00	0.75	0.88	0.96	1.00	0.00	0.86	0.94	0.98	1.00
PP	0.00	0.05	0.08	0.13	0.53	0.00	0.04	0.08	0.13	0.52
PWP	0.00	0.04	0.07	0.12	0.60	0.00	0.03	0.07	0.13	0.67

A.2 Fragmentation DAG Statistics

Table 3 describes various distributions related to the size of the approximate DAG $\mathcal{G}_{\mathcal{F}^d}$ and its associated mass set $\hat{M}(G, d, j)$ under two different parameterizations. $d = 3, j = 4$ is the configuration for FraGNNet-D3, and $d = 4, j = 4$ is the configuration for FraGNNet-D4.

Let M be the set of masses in the spectrum (peak locations), and let $M' = \hat{M}(G, d, j)$ denote the set of masses given by the approximate DAG for molecule G . Peak Recall (PR, Equation 12) is defined as the fraction of peaks in the spectrum that can be explained by a DAG mass while Peak Weighted Recall (PWR, Equation 13) incorporates peak intensities; Peak Precision (PP, Equation 14) and Peak Weighted Precision (PWP, Equation 15) are defined similarly.

$$\text{PR} = \frac{1}{|M|} \sum_{m \in M} \mathbb{I}[\exists m' \in M' : |m' - m| \leq \epsilon \max(m, 200)] \quad (12)$$

$$\text{PWR} = \sum_{m \in M} P(m) \mathbb{I}[\exists m' \in M' : |m' - m| \leq \epsilon \max(m, 200)] \quad (13)$$

$$\text{PP} = \frac{1}{|M'|} \sum_{m' \in M'} \mathbb{I}[\exists m \in M : |m' - m| \leq \epsilon \max(m, 200)] \quad (14)$$

$$\text{PWP} = \sum_{m' \in M'} P(m') \mathbb{I}[\exists m \in M : |m' - m| \leq \epsilon \max(m, 200)] \quad (15)$$

In our experiments we use a 10 ppm mass tolerance for peak matching ($\epsilon = 10^{-5}$).

A.3 Fragment Subgraph Isomorphism

In MS/MS spectrometry, it is possible for fragments with identical molecular structure to originate from different parts of the molecular graph, having been created through distinct sequences of fragmentation steps. In our model, this phenomenon is represented by pairs of DAG nodes $n_1, n_2 \in V_{\mathcal{F}^d}$ whose corresponding subgraphs $G_{n_1} \cong G_{n_2}$ are isomorphic (*i.e.*, there exists a node bijection between G_{n_1} and G_{n_2} that is both label-preserving and edge-preserving).

With the exception of $P_\theta(f)$ (which does not involve fragments), each of the latent distributions from Section 4.3 can be adapted to account for fragment graph isomorphism. To describe this process precisely, we rely on Definition A.1 and Corollary A.2:

Definition A.1. Let \mathcal{G} be a finite set of labelled graphs $\{G_i\}_{i=1}^I$. Each G_i is a member of one of K isomorphism classes $\{\mathcal{G}_k\}_{k=1}^K$, where $K \leq I$. Assume an arbitrary total ordering \prec_k for each isomorphic class \mathcal{G}_k . Let $\mathcal{I}(\mathcal{G}) \subseteq \mathcal{G}$ be the set of graphs such that $\forall G_k \in \mathcal{I}(\mathcal{G}) : \nexists G_i \in \mathcal{G} : G_i \in \mathcal{G}_k \wedge G_i \prec_k G_k$.

Corollary A.2. $\forall G_i, G_j \in \mathcal{I}(\mathcal{G}) : G_i \neq G_j \rightarrow G_i \not\cong G_j$.

For each DAG node \tilde{n} such that $G_{\tilde{n}} \in \mathcal{I}(\{G_n : n \in V_{\mathcal{F}^d}\})$, we define $P_\theta(\tilde{n})$ as the total probability of all subgraphs isomorphic to $G_{\tilde{n}}$ using Equation 16:

$$P_\theta(\tilde{n}) = \sum_{n \in V_{\mathcal{F}^d} : G_n \cong G_{\tilde{n}}} P_\theta(n) \quad (16)$$

The conditional distributions $P_\theta(f|\tilde{n})$ and $P_\theta(\tilde{n}|f)$ are defined in a similar manner using Equations 17 and 18 respectively:

$$P_\theta(f|\tilde{n}) = \sum_{n \in V_{\mathcal{F}^d} : G_n \cong G_{\tilde{n}}} \frac{P_\theta(f|n)P_\theta(n)}{P_\theta(\tilde{n})} \quad (17)$$

$$P_\theta(\tilde{n}|f) = \sum_{n \in V_{\mathcal{F}^d} : G_n \cong G_{\tilde{n}}} P_\theta(n|f) \quad (18)$$

These distributions can provide additional interpretability, as demonstrated in Appendix A.17. Intuitively, they remove excess entropy caused by uncertainty over the location in the molecule from which each fragment originated.

In practice, we calculate the set $\mathcal{I}(\{G_n : n \in V_{\mathcal{F}^d}\})$ by applying an approximate Weisfeiler-Lehman hashing algorithm (Shervashidze et al., 2011; Hagberg et al., 2008) to each subgraph $G_n : n \in V_{\mathcal{F}^d}$ and identify isomorphism class membership with hash collisions.

A.4 Molecule Features

Our method for atom and bond featurization follows the approach taken by (Goldman et al., 2024). The features are summarized in Table 4. All discrete features are encoded using a standard one-hot representation. The only continuous feature (Atom Mass) is scaled by a factor of 0.01.

Table 4: Input Features for the Molecule GNN

FEATURE	VALUES
ATOM TYPE (ELEMENT)	{C, O, N, P, S, F, Cl, Br, I, Se, Si}
ATOM DEGREE	{0, ..., 10}
ATOM ORBITAL HYBRIDIZATION	{SP, SP2, SP3, SP3D, SP3D2}
ATOM FORMAL CHARGE	{-2, ..., +2}
ATOM RADICAL STATE	{0, ..., 4}
ATOM RING MEMBERSHIP	{TRUE, FALSE}
ATOM AROMATIC	{TRUE, FALSE}
ATOM MASS	\mathbb{R}^+
ATOM CHIRALITY	{UNSPECIFIED, TETRAHEDRAL CW, TETRAHEDRAL CCW}
BOND DEGREE	{SINGLE, DOUBLE, TRIPLE, AROMATIC}

A.5 Fragment Features

A.5.1 Fourier Embeddings

We use Fourier embeddings (Goldman et al., 2023a; Tancik et al., 2020) to represent certain ordinal features such as molecular formulae and collision energy. Given an integer feature $z \in \mathbb{R}$, the corresponding Fourier embedding $\phi(z)$ can be calculated using Equation 19:

$$\phi(z) = \left[\left| \sin \left(\frac{2\pi z}{\tau_1} \right) \right|, \dots, \left| \sin \left(\frac{2\pi z}{\tau_T} \right) \right| \right] \quad (19)$$

Compared to a standard one-hot encoding scheme, this approach makes it easier for the model to handle inputs z at inference that have not been seen in training. The periods τ_t are increasing powers of 2 (we use $T = 10$ for our experiments).

A.5.2 DAG Node Features

The DAG node embeddings (Equation 4) are initialized with formula information \hat{h}_n^f and fragmentation depth information \hat{h}_n^d . The formula embedding for DAG node n is a concatenation of Fourier embeddings corresponding to heavy atom counts in G_n , described in Equation 20:

$$\hat{h}_n^f = \left\| \left\| \phi \left(\sum_{v \in V_n} \omega_v = \omega \right) \right\| \right\| \quad (20)$$

The depth embedding \hat{h}_n^d is a multi-hot representation of the fragment node’s depth in the DAG. The depth set is defined as the set of path lengths between the root node and the fragment node n , and is always a subset of $\{0, \dots, d\}$ where d is the fragmentation depth.

A.5.3 DAG Edge Features

The embeddings $\bar{h}_e^{(0)}$ are initialized for each directed edge $e \in E_{\mathcal{F}^d}$ using Equation 21. Assuming e travels from node n to node t , let $V_e = V_n - V_t$ be the set of atoms in G_n that are not in G_t . As described in Equation 22, \hat{h}_e^s is simply the average of the atom embeddings in V_e .

$$\bar{h}_e^{(0)} = \hat{h}_e^s \parallel \hat{h}_e^f \quad (21)$$

$$\hat{h}_e^s = \frac{1}{|V_e|} \sum_{a \in V_e} \bar{h}_a^{(L_1)} \quad (22)$$

The \hat{h}_e^f term is an embedding of the difference of node formulas $f_n - f_t$ using Fourier embeddings, similar to \hat{h}_n^f . These features explicitly capture neutral loss information that would otherwise need to be inferred from the DAG.

As previously noted (Section 4.4.2), for most experiments we used a version of the model that omitted DAG edges; in those cases the edge features were also not included.

A.5.4 Collision Energy Embedding

Let Z_i be the set of collision energies that were merged to create spectrum Y_i for molecule X_i in the dataset (Appendix A.10). The collision energy embedding is a representation of Z_i . Each collision energy $z \in Z_i$ is a positive integer ranging from 0 to 200 (they are normalized relative to the mass of the precursor, see Young et al. 2023 for more details). The collision energy embedding \hat{h}_Z is simply an average of Fourier embeddings for each collision energy, described by Equation 23:

$$\hat{h}_Z = \frac{1}{|Z|} \sum_{z \in Z} f(z) \quad (23)$$

The collision energy embedding \hat{h}_Z is concatenated with the output Fragment GNN embedding $\bar{h}_n^{(L_2)}$ for each DAG node $n \in G_{\mathcal{F}^d}$ before being passed to the output MLP.

A.6 Spectrum Similarity Metrics

Mass spectra are typically compared using a form of cosine similarity (Stein & Scott, 1994). The binned approach (Wei et al., 2019; Young et al., 2023; Zhu et al., 2020) involves preprocessing the spectrum by discretizing the mass range into B equally sized bins and summing the intensities for all peaks falling in the same bin. This produces a B -dimensional vector of non-negative values that is amenable to standard cosine similarity calculation. In our experiments, binned cosine similarity \mathbb{C}_{BIN} is calculated with a bin size of 0.01 Da, resulting in $B = 150,000$ (we assume a maximum mass of 1500 Da).

An alternate approach to calculating cosine similarity involves comparing intensities of peaks that are close in mass (Huber et al., 2020; Murphy et al., 2023). This method can be formalized as the linear sum assignment problem below, where i indexes spectrum Y , j indexes spectrum \hat{Y} and p_i, \hat{p}_j are shorthand for $P(m_i), \hat{P}(\hat{m}_j)$ respectively:

$$\begin{aligned} \mathbb{C}_{\text{HUN}}(Y, \hat{Y}) = \max_{w_{ij} \in \{0,1\}} \quad & \sum_{i,j} w_{ij} \frac{p_i}{\|p\|_2} \frac{\hat{p}_j}{\|\hat{p}\|_2} \\ \text{s.t.} \quad & \begin{cases} \sum_i w_{ij} \leq 1 \\ \sum_j w_{ij} \leq 1 \\ |m_i - \hat{m}_j| \leq \tau_i \end{cases} \end{aligned} \quad (24)$$

We set the tolerance parameter $\tau_i = 10^{-5} \max(m_i, 200)$ to reflect a thresholded 10 ppm mass error. As this maximization problem can be solved efficiently using the Hungarian algorithm (Kuhn, 1955), we call it *Hungarian cosine similarity*. In the literature it is sometimes referred to as *modified cosine similarity* (Huber et al., 2020). Note that the tolerance parameter only depends on the masses in spectrum Y , introducing an asymmetry in the measure. When comparing a true spectrum with a predicted spectrum (as is typically the case), we use the convention of setting Y to be the true spectrum.

A.7 Out-of-Support Prediction

Table 5: Out-of-Support (OS) Prediction performance on the NIST20 Dataset. Means and standard deviations are reported for 5 random seeds. Best scores (where applicable) are in bold.

Split	Model	$P(M^{\text{OS}})$	$P_{\theta}(M^{\text{OS}})$	$\delta_{TV}(\downarrow)$
InChIKey	FraGNNNet-D3	0.171 ± 0.000	0.191 ± 0.007	0.080 ± 0.002
InChIKey	FraGNNNet-D4	0.098 ± 0.000	0.115 ± 0.003	0.057 ± 0.001
Scaffold	FraGNNNet-D3	0.193 ± 0.000	0.213 ± 0.008	0.094 ± 0.002
Scaffold	FraGNNNet-D4	0.110 ± 0.000	0.127 ± 0.002	0.067 ± 0.001

For a given spectrum, the set of OS peak masses M^{OS} is defined using a 10 ppm mass cutoff (see Section 4.3). δ_{TV} is the total variation distance between the true OS distribution and the predicted OS distribution, given by Equation 25:

$$\delta_{TV} = |P(M^{\text{OS}}) - P_{\theta}(M^{\text{OS}})| \quad (25)$$

δ_{TV} measures how well the model can correctly predict the total OS probability. Table 5 summarizes the OS prediction performance of the FraGNNNet models. Increasing fragmentation depth from $d = 3$ to $d = 4$ resulted in both a reduction of OS peaks (lower $P(M^{\text{OS}})$) and an improved ability to approximate $P(M^{\text{OS}})$ with $P_{\theta}(M^{\text{OS}})$. This is useful since knowing $P(M^{\text{OS}})$ at inference time can help identify situations where the fragmentation algorithm performs poorly (in terms of PR and PWR, Section A.2). In such cases, it is impossible for the model to make an accurate MS/MS prediction.

A.8 Model Ablations

Table 6: FraGNNNet Model Ablations. (-CE) is removal of collision energy covariates, (+Edges) is the addition of DAG edges and associated features. Performance reported on the InChIKey test set (mean and standard deviation of 5 random seeds). Best scores are in bold.

MODEL	$\mathbb{C}_{\text{BIN}} \uparrow$	$\mathbb{C}_{\text{HUN}} \uparrow$
FraGNNNet-D3	0.721 ± 0.002	0.693 ± 0.002
FraGNNNet-D3 (-CE)	0.711 ± 0.001	0.683 ± 0.001
FraGNNNet-D3 (+Edges)	0.716 ± 0.001	0.687 ± 0.001
FraGNNNet-D4	0.736 ± 0.002	0.709 ± 0.002
FraGNNNet-D4 (-CE)	0.721 ± 0.001	0.694 ± 0.001

We performed two kinds of ablations on FraGNNNet: (-CE) corresponds to the removal of merged collision energy information (Appendix A.5.4), (+Edges) corresponds to the addition of bidirectional edges (and associated edge embeddings) and message passing in the Fragment GNN. The removal of collision energy information had a negative impact on performance, as expected. However, the addition of DAG edge information did not have a strong effect. This seems to suggest either that the hierarchical relationships between fragments (*i.e.*, nodes in the DAG) might be easy for the model to infer without DAG edges, or that this information is not helpful for making spectrum predictions.

ICEBERG (+OptFrag) is a modified version of ICEBERG that uses additional information from the ground-truth MS/MS spectrum to optimally select a set of fragments for each prediction. We emphasize that this ablation is intended solely for benchmarking purposes, since in most real-world applications the goal is to make predictions for molecules without first observing their MS/MS spectra. Providing ICEBERG with this additional information resulted in improved performance that nearly matched that of FraGNNNet-D4 (Table 7).

Table 7: ICEBERG Model Ablations. (+OptFrag) replaces stochastic fragment generation with an optimal approach that uses information from the ground-truth MS/MS spectrum. Performance reported on both InChIKey and Scaffold test sets (mean and standard deviation of 5 random seeds). Best scores are in bold.

MODEL	INCHIKEY $\mathbb{C}_{\text{BIN}} \uparrow$	SCAFFOLD $\mathbb{C}_{\text{BIN}} \uparrow$
FRAGNNET-D4	0.736 ± 0.002	0.678 ± 0.005
ICEBERG	0.707 ± 0.001	0.636 ± 0.002
ICEBERG (+OPTFRAG)	0.732 ± 0.000	0.668 ± 0.002

A.9 Datasets and Splits

We trained and evaluated all models on the NIST 2020 MS/MS dataset (Stein, 2012; Yang et al., 2014), a large commercial library of MS data. To ensure homogeneity, the original dataset was filtered to include only $[\text{M}+\text{H}]^+$ adducts. Following (Goldman et al., 2023a; 2024), spectra for the same compound acquired at different collision energies were combined (a process commonly referred to as *collision energy merging*, see Appendix A.10). The resulting dataset contained 21,113 unique molecules, each with an associated merged MS/MS spectrum. Models were trained using 60% of the data, with 20% for validation and 20% used as a heldout test set. Two strategies for data splitting were employed: a simple random split by molecule ID using the InChIKey hashing algorithm (Heller et al., 2015), and a more challenging split that clustered molecules based on their Murcko Scaffold (a coarse representation of 2D molecular structure, Bemis & Murcko 1996). Scaffold splits are commonly used to evaluate generalization of deep learning models in cheminformatics applications (Wu et al., 2018).

A.10 Data Preprocessing

We exported spectra from the NIST20 MS/MS spectral library (following this github repository). We applied a number of filters based on the spectral metadata and molecular properties.

The metadata criteria are described below:

- Orbitrap instrument with higher-energy collisional dissociation (HCD)
- $[\text{M}+\text{H}]^+$ adduct type
- Precursor $m/z \leq 1500$
- Normalized collision energy

The molecule criteria are described below:

- Element composition: H, C, O, N, P, S, F, Cl, Br, I, Se, Si
- ≤ 60 heavy (non-H) atoms
- ≤ 240 bonds between heavy atoms
- Neutral charge
- No radical electrons
- Single molecule

After filtering, there were 262,319 spectra representing 21,113 molecules.

Individual MS/MS spectra for the same molecule and precursor adduct were merged across collision energies by averaging the mass distributions. More formally, let $\{Y^{(i)}\}_{i=1}^I$ be the set of spectra corresponding to molecule X (each measured with a different collision energy Z_i). The merged spectrum Y is defined using Equation 26.

$$Y = \bigcup_{i=1}^I \left\{ \left(m_j^{(i)}, \frac{P(m_j^{(i)})}{I} \right) \right\}_j^{(i)} \quad (26)$$

A.11 Compound Retrieval Continued

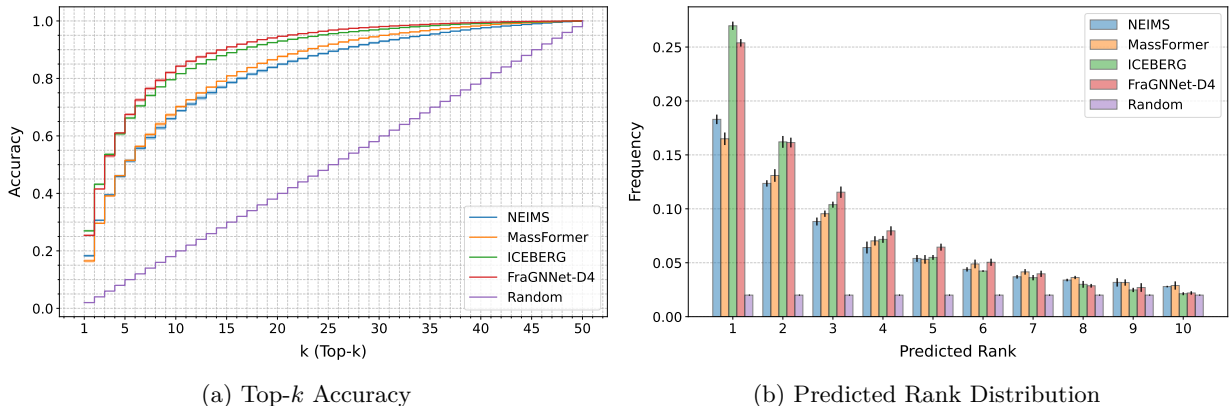


Figure 7: Compound retrieval results on the InChIKey split: (a) Top- k Accuracy for all values $1 \leq k \leq 50$ and (b) Predicted Rank Distribution over ranks 1-10. Mean over 5 seeds is reported; error bars indicate standard deviation.

The retrieval results on the InChIKey split (Figure 7) are largely consistent with the results on the Scaffold split (Figure 4), although ICEBERG does perform better in terms of top- k accuracy for $k = 1$ and $k = 2$. All models perform slightly better on the InChIKey split than they do on the Scaffold split, as expected.

A.12 Implementation Details

The FraGNNet model and baselines were implemented in Python (Python Core Team 2021, version 3.10.13), using Pytorch (Paszke et al. 2019, version 2.1.0, CUDA 11.8) and Pytorch Lightning (Falcon & The PyTorch Lightning team 2019, version 2.1.2). Weights and Biases (Biewald 2020, version 0.16.1) was used to track experiments and run hyperparameter sweeps. The recursive fragmentation algorithm was implemented in Cython (Behnel et al. 2011, version 3.0.6). The graph neural network modules were implemented using Pytorch Geometric (Fey & Lenssen 2019, version 2.4.0). The data preprocessing and molecule featurization used RDKit (Landrum 2022, version 2022.09.4).

A.13 Parameter Counts

The parameter counts for all models are summarized in Table 8.

A.14 Baseline Models

All baseline models were re-implemented in our framework, to facilitate fair comparison across methods. Some of the models were originally designed to support additional covariates such as precursor adduct and instrument type. Since our experiments were restricted to MS/MS data of a single precursor adduct ($[M+H]^+$) and instrument type (Orbitrap), we excluded these features in our implementations.

Table 8: Parameter counts, reported in millions.

MODEL	# PARAMETERS
FraGNNET-D4	1.6
FraGNNET-D3	1.2
ICEBERG	17.6
MASSFORMER	165.3
NEIMS	125.4
GRAFF-MS	57.8

A.14.1 ICEBERG

ICEBERG (Inferring Collision-induced-dissociation by Estimating Breakage Events and Reconstructing their Graphs, Goldman et al. 2024) is a state-of-the-art C2MS model. ICEBERG is composed of two sub-modules (neural networks) that are trained independently of each other. The first module (the *fragment generator*) autoregressively predicts a simplified fragmentation DAG, and the second module (the *intensity predictor*) outputs a distribution over those fragments. The fragment generator is trained to approximate a fragmentation tree that is constructed using a variant of the MAGMa algorithm (Ridder et al., 2014). MAGMa applies a combinatorial atom removal strategy to generate a fragmentation DAG from an input molecular graph G : the resulting MAGMa DAG has a similar set of fragment nodes to $G_{\mathcal{F}d}$, but may contain different edges (refer to Ridder et al. 2014; Goldman et al. 2024 for full details). The MAGMa DAG is then simplified using a number of pruning strategies. Fragments with masses that are not represented by any peak in the spectrum are removed, as are fragments that map to same peak as another (chemical heuristics are used to determine which fragment should be kept in such cases). Unlike our approach, no distinction is made between isomorphic fragments that originate from different parts of the molecule. Redundant paths between fragments are removed to convert the DAG into a proper tree, which is required for autoregressive generation.

The aggressive DAG pruning removes information that could be important for correctly predicting the spectrum. However, this pruning also facilitates more expressive representations of the fragments that remain: since the total number of fragments is lower, the computational and memory cost per fragment can be much higher. This tradeoff underlines the key conceptual difference between FraGNNet and ICEBERG. The former uses a more complete fragmentation DAG but must employ a simpler representation for each individual fragment. The latter can afford a more complex fragment representation but only considers a sampled subset of the DAG.

In ICEBERG the output spectrum is binned, with each fragment contributing to the intensity of a particular bin (refer to Goldman et al. 2024, Section 2.5 for full details). Unlike FraGNNet, ICEBERG does not explicitly model a latent fragment distribution $P_{\theta}(n)$ or formula distribution $P_{\theta}(f)$. There is no straightforward method to calculate these latent distributions in a way that is consistent with the output spectrum.

ICEBERG (+OptFrag) is a variant of ICEBERG that we introduced for the purposes of benchmarking (Section A.8). ICEBERG (+OptFrag) replaces stochastic fragment generation (*i.e.*, the first module) with the exact output of the MAGMa algorithm. This modification removes sampling error in the fragment generation process, creating an artificially easier learning problem that should result in better performance. However, it assumes access to the ground truth MS/MS spectrum for the input molecule. ICEBERG (+OptFrag) is helpful in benchmarking because it can be used to infer how much overall MS/MS prediction error is caused by incorrect fragment generation, but it is not practically useful as a C2MS model.

Our ICEBERG implementation was based on the code from Goldman et al. 2024, although in our experiments the model was trained using binned cosine similarity with 0.01 Da bins (previously, it was trained using 0.1 Da bins). We applied a square root transformation to each binned target intensity during training. We also fixed a bug that caused spurious peaks to appear in the smallest m/z bin as a result of improper batching.

A.14.2 GrAFF-MS

GrAFF-MS (Graph neural network for Approximation via Fixed Formulas of Mass Spectra, Murphy et al. 2023) is a structured C2MS model. Unlike ICEBERG and FraGNet, GrAFF-MS does not rely on fragment information, instead predicting a distribution over formulae $P_\theta(f)$ directly. It uses a static library of common product and neutral loss formulae derived from the formula annotations of a labelled spectrum dataset. At inference time, the model predicts a distribution over the formula library, and the formula masses are used to map this distribution to a spectrum.

In our experiments we used the NIST20 expert-curated formula annotations to construct the formula library (see Appendix A.15 for details). Each formula annotation f in the dataset can be interpreted as a product formula $f^+ = f$; the associated neutral loss formula can be calculated as $f^- = p - f$, where p is the precursor formula for that spectrum. For each formula annotation in the dataset, we recorded its associated peak intensity. In the case of multiple formula annotations for the same peak, we divided the peak intensity equally across all annotations. We then selected the top 10,000 product and neutral loss formulae in terms of total intensity across spectra in the dataset. Given a molecule with precursor formula p , the support of the formula distribution $P_\theta(f)$ is defined as the union of the set of product formulae $\{f_i^+\}_i$ and the set of complements of the neutral loss formulae $\{p - f_j^-\}_j$.

We trained the model with a peak-marginal cross-entropy loss (Murphy et al., 2023) using a 10 ppm mass tolerance (to be consistent with our C_{HUN} metric). The original GrAFF-MS implementation was designed to work with a single collision energy; our implementation uses the average collision energy to predict the merged spectrum. Like the original model, our implementation supports isotopic traces for each predicted peak, modelled as an additional covariate (*i.e.*, binary variable indicating presence/absence of isotopes). This sort of isotope information is present in the NIST20 MS/MS dataset, although it is not used for FraGNet or the other baseline models.

A.14.3 NEIMS

NEIMS (Neural Electron Ionization Mass Spectrometry, Wei et al. 2019) was the first deep learning C2MS model, originally designed for low mass accuracy (1.0 Da bins) electron-ionization mass spectrometry (EI-MS) prediction. NEIMS represents the input molecule using a domain-specific featurization method called a molecular fingerprint, which capture useful properties of the molecule such as the presence or absence of various substructures. More recent works (Zhu et al., 2020; Young et al., 2023; Goldman et al., 2023a) have adapted NEIMS to ESI-MS/MS prediction at higher mass accuracy (0.1 Da bins). We based our implementation on the version from Young et al. 2023 which uses three different kinds of molecular fingerprint representations: the Extended Connectivity (Morgan) fingerprint (Rogers & Hahn, 2010), the RDKit fingerprint (Landrum, 2022), and the Molecular Access Systems (MACCS) fingerprint (Durant et al., 2002). We adapted the model to use the same collision energy featurization strategy as FraGNet (Equation 23). Finally, to avoid an excess of parameters, we replaced the final fully-connected layer’s weight matrix with a low-rank approximation. This layer maps from the latent dimension $d_h = 1024$ to the output dimension $d_o = 150000$, corresponding to the mass range $[0, 1500]$ with 0.01 Da bins. The low-rank approximation was implemented as product of two learnable weight matrices: a $d_h \times d_r$ matrix and a $d_r \times d_o$ matrix, where $d_r = 256$.

We trained the model with binned cosine similarity, and applied a square root transformation to the binned target intensities.

A.14.4 MassFormer

MassFormer (Young et al., 2023) is a binned C2MS method that was originally designed for low mass accuracy (1.0 Da bins) MS/MS prediction. It uses a graph transformer architecture (Ying et al., 2021) that is pre-trained on a large chemical dataset (Nakata & Shimazaki, 2017) and then fine-tuned on spectrum prediction. We preserved most aspects of the model’s original implementation but adapted the collision energy featurization and low rank output matrix approximation ($d_r = 128$) from the NEIMS baseline. Unlike the original MassFormer paper, we did not employ FLAG (Kong et al., 2022), a strategy for adversarial data

augmentation in graphs, since none of the other models used data augmentation. We trained the model with binned cosine similarity, and applied a square root transformation to the binned target intensities.

A.14.5 Precursor-Only

A trivial baseline that simply puts 100% of the intensity on the precursor peak. More formally, given the input molecule’s precursor formula p , the model predicts a spectrum with a single peak $\{(\text{mass}(p), 1)\}$. This baseline is useful because the precursor peak typically accounts for a large fraction of the overall intensity in the spectrum.

A.15 Formula Annotation Evaluation

The NIST20 ground-truth formula annotations were determined using a combination of algorithmic and manual approaches. Following (Murphy et al., 2023), we excluded glycan and peptide spectra from our formula annotation analysis and focused on small molecules.

Based on our correspondence with scientists at NIST, the procedure for establishing small molecule formula annotations can be described as follows. For each precursor compound, an exhaustive decomposition of the precursor molecular formula was used to enumerate all possible subformulae. These subformulae were then matched to peaks in the spectrum by comparing exact subformula masses with measured peak masses. Finally, expert opinion was used to remove unlikely annotations.

While the details of the matching process are not published, our analysis indicates that the vast majority ($\approx 95\%$) of formula annotation masses were within 10 ppm of their associated real peak masses. A small fraction of annotation formula masses ($< 1\%$) are within 10 ppm of at least one other peak in the spectrum. For consistency with the peak matching metrics used elsewhere in the paper (*i.e.*, the Hungarian cosine similarity metric C_{HUN} , Appendix A.6), we excluded annotations with formula masses more than 10 ppm away from their associated peak mass.

The annotation metrics used in Section 5.3 are defined in the following equations; $\epsilon = 10^{-5}$ is the mass tolerance parameter.

$$\text{AR} = \frac{\sum_{m \in M} \mathbb{I}[\exists m' \in M' : (|m - m'| \leq \epsilon \max(m, 200)) \wedge (|A(m) \wedge A(m')| > 0)]}{\sum_{m \in M} \mathbb{I}[|A(m)| > 0]} \quad (27)$$

$$\text{AWR} = \frac{\sum_{m \in M} P(m) \mathbb{I}[\exists m' \in M' : (|m - m'| \leq \epsilon \max(m, 200)) \wedge (|A(m) \wedge A(m')| > 0)]}{\sum_{m \in M} P(m) \mathbb{I}[|A(m)| > 0]} \quad (28)$$

$$\text{AP} = \frac{\sum_{m' \in M'} \mathbb{I}[\exists m \in M : (|m - m'| \leq \epsilon \max(m, 200)) \wedge (|A(m) \wedge A(m')| > 0)]}{\sum_{m' \in M'} \mathbb{I}[|A(m')| > 0]} \quad (29)$$

$$\text{AWP} = \frac{\sum_{m' \in M'} P_{\theta}(m') \mathbb{I}[\exists m \in M : (|m - m'| \leq \epsilon \max(m, 200)) \wedge (|A(m) \wedge A(m')| > 0)]}{\sum_{m' \in M'} P_{\theta}(m') \mathbb{I}[|A(m')| > 0]} \quad (30)$$

$$\text{AF1} = \frac{2}{\text{AR}^{-1} + \text{AP}^{-1}} \quad (31)$$

$$\text{AWF1} = \frac{2}{\text{AWR}^{-1} + \text{AWP}^{-1}} \quad (32)$$

Note that with FraGNNNet and GrAFF-MS, the formula annotations for a given input molecule are deterministically computed: in the former case they derived from the fragmentation DAG \mathcal{F}^d , while in the latter they are given by a static formula library. In both cases, the model’s learned parameters only affect predicted peak intensities, not formula annotations. In contrast, ICEBERG uses a learned model to predict both formula

annotations and peak intensities. This explains why seed variance for FraGNNNet and GrAFF-MS is only reported in Table 2 for metrics that involve predicted intensities (AWP, AWF1).

In the case of the ICEBERG model, the metrics AWP or AWF1 are not well defined due to their dependence on predicted peak intensities. Unlike the other models, ICEBERG peak intensities $P_\theta(m')$ are only calculated after a 0.01 Da mass binning. This makes it impossible to evaluate $P_\theta(m'_1)$ and $P_\theta(m'_2)$ for predicted peaks m'_1 and m'_2 that end up in the same mass bin. For ICEBERG, the other metrics in Table 2 are calculated using the unbinned formula masses, *i.e.*, $m'_i = \text{mass}(f^i)$ for each predicted formula f^i .

A.16 Ensembling

Let $\{\theta^k : \theta^k \sim P(\theta)\}_{k=1}^K$ denote the set of parameters for an ensemble of K models with the same architecture, sampled IID from a distribution over parameters $P(\theta)$. We perform ensembling in the latent space, using Equations 33 and 34 to calculate the ensemble latent distributions $P_\theta^K(n|f)$ and $P_\theta^K(f)$ (respectively):

$$P_\theta^K(n|f) = \frac{1}{K} \sum_k P_\theta^k(n|f) \approx \bar{P}(n|f) = \mathbb{E}_{\theta \sim P(\theta)} [P_\theta(n|f)] \quad (33)$$

$$P_\theta^K(f) = \frac{1}{K} \sum_k P_\theta^k(f) \approx \bar{P}(f) = \mathbb{E}_{\theta \sim P(\theta)} [P_\theta(f)] \quad (34)$$

Note that ensembling in this way results in spectrum predictions that are the average of the individual model predictions (Equation 35):

$$P_\theta^K(m) = \frac{1}{K} \sum_k P_\theta^k(m) \approx \bar{P}(m) = \mathbb{E}_{\theta \sim P(\theta)} [P_\theta(m)] \quad (35)$$

Let $H_\theta^K(N|f)$ denote the entropy of $P_\theta^K(n|f)$. Note that $H_\theta^K(N|f)$ is a Monte Carlo approximation of $\bar{H}(N|f) = \mathbb{E}_{n \sim \bar{P}(n|f)} [-\log \bar{P}(n|f)]$.

We want to show that ensembling increases latent conditional entropy. This is formalized in Equation 36:

$$\mathbb{E}_{\theta \sim P(\theta)} [H_\theta(N|f)] \leq \bar{H}(N|f) \quad (36)$$

Proof. Proving Equation 36 simply requires noting that entropy is strictly concave with respect to the probability density function. To make this clear, we introduce the notation $h(P(x)) = H(X)$ where h is the entropy function applied to the distribution $P(x)$.

$$\begin{aligned} \bar{H}(N|f) &= h(\bar{P}(n|f)) \\ &= h(\mathbb{E}_{\theta \sim P(\theta)} [P_\theta(n|f)]) \\ &\geq \mathbb{E}_{\theta \sim P(\theta)} [h(P_\theta(n|f))] \\ &= \mathbb{E}_{\theta \sim P(\theta)} [H_\theta(N|f)] \end{aligned}$$

□

By the same reasoning we can get bounds for the isomorphic distributions (Equation 37):

$$\mathbb{E}_{\theta \sim P(\theta)} [H_\theta(\tilde{N}|f)] \leq \bar{H}(\tilde{N}|f) \quad (37)$$

Since normalized entropy is simply a scaled version of entropy, the inequalities in Equations 36 and 37 also hold if each entropy is replaced with its normalized counterpart.

A.17 Isomorphic Fragment Annotation

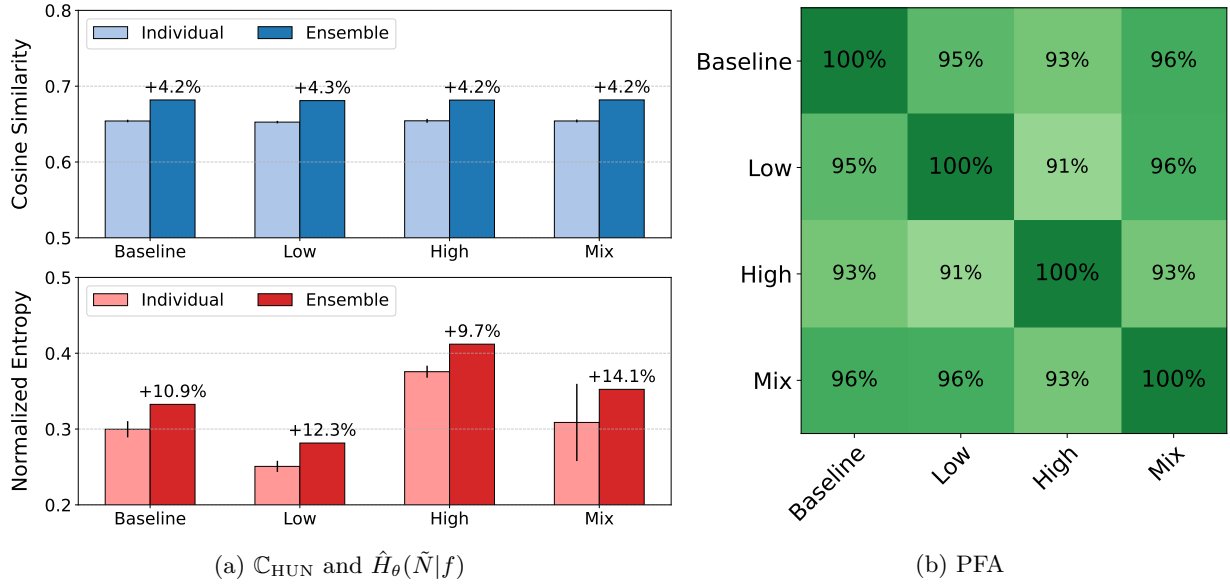


Figure 8: (a) For each ensemble configuration (Baseline, Low, High, Mix), the cosine similarity \mathbb{C}_{HUN} and normalized entropy of the annotation distribution $\hat{H}_{\theta}(\tilde{N}|f)$ are reported. For both metrics, the average score of the individual models (Individual) is compared with the score of the ensemble (Ensemble). Each ensemble consists of $K = 15$ models. Standard deviations for the K individual models are plotted as error bars. (b) Pairwise fragment annotation agreement (PFA) for all ensemble combinations are plotted in a matrix. The consensus agreement (CFA) is $\approx 89\%$.

For a given pair of ensembles $P_{\theta_1}^K$ and $P_{\theta_2}^K$, pairwise fragment annotation agreement (PFA) measures the average amount of mode agreement between their fragment annotation distributions $P_{\theta_1}^K(n|f)$ and $P_{\theta_2}^K(n|f)$. More formally, let F_i be the set of formula annotations in a predicted MS/MS spectrum i . PFA is defined using Equation 38.

$$\text{PFA} = \frac{1}{I} \sum_i \frac{\sum_{f \in F_i} \mathbb{I}[\arg \max_{\tilde{n}} P_{\theta_1}^K(\tilde{n}|f) = \arg \max_{\tilde{n}} P_{\theta_2}^K(\tilde{n}|f)]}{|F_i|} \quad (38)$$

Consensus fragment annotation agreement (CFA, Equation 39) is similar to PFA but measures agreement across all ensembles.

$$\text{CFA} = \frac{1}{I} \sum_i \frac{\sum_{f \in F_i} \mathbb{I}[\bigwedge_{a,b} (\arg \max_{\tilde{n}} P_{\theta_a}^K(\tilde{n}|f) = \arg \max_{\tilde{n}} P_{\theta_b}^K(\tilde{n}|f))]}{|F_i|} \quad (39)$$

Figure 8 presents the same experiments as those covered by Figure 5, but focusing on the isomorphic annotation distribution $P_{\theta}(\tilde{n}|f)$ instead of $P_{\theta}(n|f)$. The general trends are the same: ensembling increases both cosine similarity and normalized entropy, PFA is $\geq 91\%$, and CFA is $\approx 89\%$. Note that for each ensemble configuration, $H_{\theta}(\tilde{N}|f) < H_{\theta}(N|f)$; this makes sense, as one would expect $P_{\theta}(\tilde{n}|f)$ to be more concentrated than $P_{\theta}(n|f)$ since the former does not distinguish between isomeric fragments.

Note that cases where only a single fragment is possible (*i.e.*, formulae $f \in F_i$ such that $P_{\theta}^K(n|f)$ is a degenerate distribution) are excluded from our analysis.

A.18 Hyperparameter Optimization

For each model, we ran a random hyperparameter sweep with a budget of 100 samples on the InChIKey split, and selected the configuration with the best validation performance as measured by binned cosine similarity \mathbb{C}_{BIN} . The specific parameters that were optimized varied depending on the type of model.